

A Numerical Study of the 2-Flavour Schwinger Model with Dynamical Overlap Hypercube Fermions

Wolfgang Bietenholz^a, Ivan Hip^b,
Stanislav Shcheredin^c and Jan Volkholz^d

^a Instituto de Ciencias Nucleares
Universidad Nacional Autónoma de México
A.P. 70-543, C.P. 04510 Distrito Federal, Mexico

^b Faculty of Geotechnical Engineering, University of Zagreb
Hallerova aleja 7, 42000 Varaždin, Croatia

^c Fakultät für Physik, Universität Bielefeld
D-33615 Bielefeld, Germany

^d Potsdam Institute for Climate Impact Research
Telegrafenberg A62, D-14412 Potsdam, Germany

We present numerical results for the 2-flavour Schwinger model with dynamical chiral lattice fermions. We insert an approximately chiral hypercube Dirac operator into the overlap formula to construct the overlap hypercube operator. This is an exact solution to the Ginsparg-Wilson relation, with an excellent level of locality and scaling. Due to its similarity with the hypercubic kernel, a low polynomial in this kernel provides a numerically efficient Hybrid Monte Carlo force. We measure the microscopic Dirac spectrum and discuss the corresponding scale-invariant parameter, which takes a surprising form. This is an interesting case, since Random Matrix Theory is unexplored for this setting, where the chiral condensate Σ vanishes in the chiral limit. We also measure Σ and the “pion” mass, in distinct topological sectors. In this context we discuss and probe the topological summation of observables by various methods, as well as the evaluation of the topological susceptibility. The feasibility of this summation is essential for the prospects of dynamical overlap fermions in QCD.

Contents

1	The Schwinger model	2
2	Lattice formulation with overlap Hypercube Fermions	5
3	Hybrid Monte Carlo with a preconditioned force	11
3.1	Algorithm	11
3.2	Statistics	13
3.3	Reversibility, acceptance rate and computational effort . . .	14
4	The Dirac spectrum	16
4.1	Unfolded level spacing distribution	16
4.2	The microscopic Dirac spectrum	21
4.3	Eigenvalues in the bulk of the Dirac spectrum	25
5	Topological summation and susceptibility	26
5.1	Gaussian evaluation of the topological susceptibility	27
5.2	An approximate formula for the topological summation . . .	30
5.3	Topological summation of the chiral condensate	32
5.4	Topological summation of the “pion” mass	35
5.5	Correlation of the topological charge density	37
6	Conclusions	38

1 The Schwinger model

The Schwinger model describes QED in two dimensions, *i.e.* 2-component Dirac fermions interacting through a $U(1)$ gauge field [1]. In a Euclidean plane, the Lagrangian reads

$$\mathcal{L}(\bar{\psi}, \psi, A_\mu) = \bar{\psi}(x) \left[\gamma_\mu (i\partial_\mu + gA_\mu(x)) + m \right] \psi(x) + \frac{1}{2} F_{\mu\nu}(x) F_{\mu\nu}(x) . \quad (1.1)$$

It is a popular toy model for QCD; in particular it shares the property of confinement [1, 2]. On the other hand there are fundamental differences, such as the super-renormalisability of the Schwinger model, and a non-running gauge coupling g .

A further qualitative difference — which is of particular interest in this work — is the spontaneous chiral symmetry breaking in QCD with massless quarks. In $d = 2$ this effect can be mimicked to some extent for instance by the Gross-Neveu model, where a discrete chiral symmetry breaks spontaneously. However, in the Schwinger model with fermion mass $m = 0$ the

chiral symmetry is continuous, and therefore it cannot undergo spontaneous symmetry breaking (SSB) due to the Mermin-Wagner Theorem [3]. Nevertheless the chiral condensate $\Sigma = -\langle\bar{\psi}\psi\rangle$, which acts as the order parameter for chiral symmetry breaking, takes a non-vanishing value in the 1-flavour case, because of the explicit symmetry breaking due to the axial anomaly [1]. This leads to $\Sigma(m=0) = (e^\gamma/2\pi^{3/2})g \simeq 0.16g$ (where γ is Euler's constant).

For $N_f \geq 2$, however, the massless limit has an *unbroken* chiral symmetry. For N_f degenerate fermion flavours of mass m the chiral condensate behaves as [4]

$$\Sigma(m) \propto \left(\frac{m^{N_f-1}}{\beta}\right)^{1/(N_f+1)} \Rightarrow \delta = \frac{N_f+1}{N_f-1}, \quad (1.2)$$

where $\beta = 1/g^2$, and δ is the critical exponent.

In our study we consider $N_f = 2$. Here there are analytical evaluations of the proportionality constant for the case of light fermions, $m \ll g$, based on bosonisation and low energy assumptions,

$$\Sigma(m) = \text{const.} \left(\frac{m}{\beta}\right)^{1/3}, \quad \text{const.} = \begin{cases} 0.372\dots & \text{Ref. [5]} \\ 0.388\dots & \text{Ref. [6]} \end{cases}. \quad (1.3)$$

Under the same assumptions the mass of the iso-triplet (“pion”) [6] and of the iso-singlet (“ η particle”) [7] are predicted as

$$M_\pi = 2.008\dots(m^2g)^{1/3}, \quad M_\eta = \sqrt{M_\pi^2 + \frac{2g^2}{\pi}}. \quad (1.4)$$

The relation $M_\pi \propto m^{2/3}$ replaces the Gell-Mann–Oakes–Renner relation ($M_\pi \propto \sqrt{m}$) of QCD [8].

For models with a finite condensate $\Sigma(m=0)$, its value can be determined from the Banks-Casher plateau of the Dirac eigenvalue density at zero [9] (or near zero in a finite volume). Moreover, chiral Random Matrix Theory (RMT) has elaborated subtle techniques to predict a wiggle structure on this plateau, which allows for a refined determination of Σ from the densities of the low-lying Dirac eigenvalues [10, 11]. This method has been tested successfully in the ϵ -regime of QCD with quenched [12–14]¹ and with dynamical [16, 17] quarks, and also in the 1-flavour Schwinger model [18, 19]. The latter studies were based on configurations, which were

¹Strictly speaking Σ diverges logarithmically for increasing volume in the quenched approximation [15]. Still quenched QCD in boxes of length $\gtrsim 1.2$ fm yields sensible results for the chiral condensate.

generated quenched and later re-weighted with the fermion determinant; we denote this method as “quenched re-weighted”.²

However, the established RMT techniques are not applicable in the chiral limit of the 2-flavour Schwinger model; RMT for situations with $\Sigma(m=0)=0$ awaits to be worked out. Nevertheless we confirm the usual RMT prediction for the unfolded level spacing distribution in a unitary ensemble. On the other hand, the microscopic spectrum does not exhibit a Banks-Casher plateau. Instead we observe to high precision the scale-invariance of the product $\lambda V^{5/8}$, where λ is a low-lying Dirac eigenvalue in the volume V . This result remains to be understood from the RMT perspective, since it cannot be explained simply with the critical exponent $\delta=3$ given in eq. (1.2). We also discuss the densities of the Dirac eigenvalues in the bulk and their scaling behaviour.

Next we confront the measurement of $\Sigma(m)$, based on the full Dirac spectrum, with eq. (1.3). This requires an (approximate) summation of the values in all topological sectors, guided by the measurements in a few sectors. We probe several methods for this purpose and apply them to Σ and to the “pion” mass given in eq. (1.4). These approaches also involve a determination of the topological susceptibility. The requirement of a topological summation is generic for simulations with dynamical chiral fermions, because the Monte Carlo histories tend to perform only very few topological transitions. Also other lattice fermion formulations, such as the Wilson fermion and variants thereof, will run into the same problem when they represent light fermions on very fine lattices [22] (say $a \lesssim 0.05$ fm in QCD). Therefore the applicability of these techniques is relevant, particularly in view of QCD simulations with light quarks close to the continuum limit.

Section 2 describes our lattice formulation of the Schwinger model and discusses some of its properties, in particular locality and scaling. Section 3 presents our version of the Hybrid Monte Carlo algorithm which we used in this study. We discuss its properties regarding conceptual conditions, and practical aspects of its performance. Section 4 deals with the Dirac spectrum, the construction of a scale-invariant variable and the link to RMT. Section 5 discusses the summation of Σ and M_π over the topological sectors, along with the evaluation of the topological susceptibility. Section 6 is devoted to our conclusions. Progress reports of this project have appeared in several proceeding contributions [23].

²That method was pioneered in the Schwinger model in Ref. [20]. It worked successfully in some cases, but it runs into trouble when the fermion determinant fluctuates strongly, as it happens for very light fermions. Hence the study presented here requires the simulation of truly dynamical fermions, as it was first attempted in Ref. [21].

2 Lattice formulation with overlap Hypercube Fermions

We consider the lattice formulation of the Schwinger model with compact link variables $U_{x,\mu} \in U(1)$, and with the plaquette gauge action. Remarkably, for the pure gauge theory this is indeed a perfect lattice action [24]. For the fermions we employ an overlap hypercube fermion (overlap-HF) Dirac operator, which is an exact solution to the Ginsparg-Wilson Relation (GWR).

The GWR is a criterion for a lattice modified, exact chiral symmetry [25], which first emerged from the study of perfect actions for lattice fermions [24, 26–28]. Independently, chiral lattice fermions were constructed in the Domain Wall Fermion formulation [29], which separates the zero modes of opposite chirality in an extra “dimension”.³ Integrating out this extra direction leads to the overlap formula [30], which provides yet another way to represent a chiral vector theory on the lattice [31]. The lattice Dirac operator for Domain Wall Fermions (in the limit of an infinite wall separation) and for overlap fermions turned out to be solutions to the GWR as well [31].

Its importance as a general chirality criterion was first pointed out in Refs. [28], which showed in addition that classically perfect fermion actions obey this criterion as well. Since those formulations involve couplings over an infinite range (in $d > 1$), a truncation is needed, which marginally distorts the perfect symmetry and scaling properties. For the free, optimally local, perfect fermion [24] the truncation to a unit hypercube by means of periodic boundary conditions over three lattice spacings preserves excellent scaling [32] and chirality [33]. It leads to a lattice Dirac operator of the form

$$D_{\text{HF}}(x, x+r) = \rho_\mu(r)\gamma_\mu + \lambda(r) , \quad (2.1)$$

i.e. a vector term plus a scalar term, as in the case of the Wilson fermion, but with an extended structure (x and $x+r$ are lattice sites).

In $d = 2$ these terms include only couplings to nearest neighbour lattice sites and across the plaquette diagonals. We are using here the version denoted as CO-HF (Chirally Optimised Hypercube Fermion) in Ref. [34], which is optimal for our algorithm to be described in Section 3. For convenience we display in Table 1 the couplings in the notation of eq. (2.1).

We gauge D_{HF} by multiplying the compact link variables along the shortest lattice paths connecting x and $y = x+r$; for the diagonal the two shortest paths are averaged [34]. Thus we arrive at the operator $D_{\text{HF},xy}(U)$,

³An extra direction is introduced, which appears as a dimension for the free fermion, but which does not carry gauge fields.

r	$\rho_1(r)$	$\lambda(r)$
(0, 0)	0	1.49090692
(1, 0)	0.30583220	-0.24771369
(1, 1)	0.09708390	-0.12501304

Table 1: *The coupling constants of the Chirally Optimised Hypercube Fermion (CO-HF) [34]. Note that $\rho_1(r)$ is even in r_1 and odd in r_2 (and vice versa for $\rho_2(r)$), while $\lambda(r)$ is even in both components of r .*

which characterises the interacting Hypercube Fermion (HF).

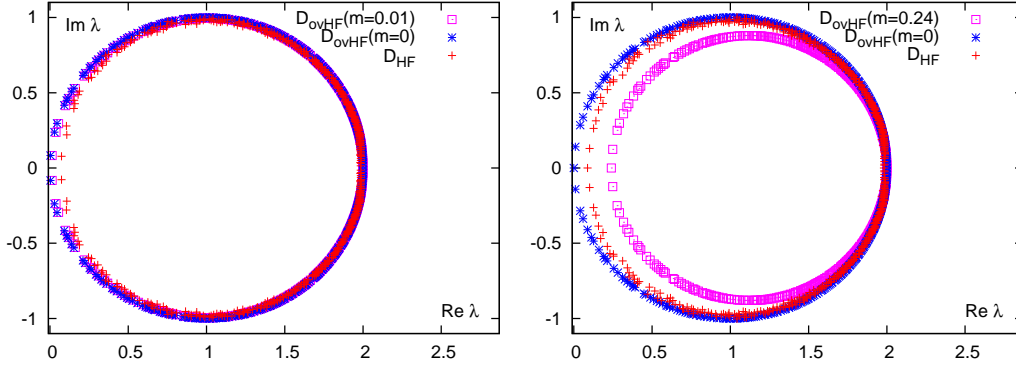


Figure 1: *The spectra of D_{HF} and of D_{ovHF} (with and without mass) in the complex plane, for a typical configuration generated at $\beta = 5$ on a 16×16 lattice with $m = 0.01$ (on the left) and at $m = 0.24$ (on the right). The similarity of D_{HF} to $D_{\text{ovHF}}^{(0)}$ and to $D_{\text{ovHF}}(m)$ shows that the HF is approximately chiral, and useful for an efficient computation of the Hybrid Monte Carlo force (see Section 3).*

Since the operator D_{HF} is “ γ_3 -Hermitian”, $D_{\text{HF}}^\dagger = \gamma_3 D_{\text{HF}} \gamma_3$, the exact chirality (which got lost in the truncation) can be restored by inserting D_{HF} into the overlap formula [31]. This yields the overlap-HF operator [33, 34]

$$\begin{aligned}
D_{\text{ovHF}}(m) &= \left(1 - \frac{m}{2}\right) D_{\text{ovHF}}^{(0)} + m, \\
D_{\text{ovHF}}^{(0)} &= 1 + \gamma_3 \frac{H_{\text{HF}}}{\sqrt{H_{\text{HF}}^2}}, \quad H_{\text{HF}} = \gamma_3 (D_{\text{HF}} - 1). \quad (2.2)
\end{aligned}$$

H_{HF} is Hermitian⁴ and $D_{\text{ovHF}}^{(0)}$ fulfils the GWR in its simplest form,

$$\{D_{\text{ovHF}}^{(0)}, \gamma_3\} = D_{\text{ovHF}}^{(0)} \gamma_3 D_{\text{ovHF}}^{(0)}. \quad (2.3)$$

⁴The constant 1 in the formulation of H_{HF} is fine since we deal with smooth gauge configurations. For stronger gauge couplings one would prefer to increase this constant.

In practice we evaluate this overlap operator by means of rational Zolotarev polynomials, as suggested in Ref. [35], after projecting out the lowest two modes of $D_{\text{HF}}^\dagger D_{\text{HF}}$, which are treated separately.

Compared to H. Neuberger's standard overlap operator D_{N} [31], we replace the Wilson kernel D_{W} by D_{HF} [33]. Since the latter is an approximate solution to the GWR already, the transition $D_{\text{HF}} \rightarrow D_{\text{ovHF}}$ is only a modest *chiral correction*,

$$D_{\text{ovHF}} \approx D_{\text{HF}} , \quad (2.4)$$

in contrast to the drastic transition $D_{\text{W}} \rightarrow D_{\text{N}}$. This property is illustrated in Figure 1, which compares the spectra of D_{HF} and D_{ovHF} for typical gauge configurations generated at $m = 0.01$ and at $m = 0.24$, both at $\beta = 5$ on a 16×16 lattice. The similarity of D_{HF} to $D_{\text{ovHF}}^{(0)}$ is useful for the computation of the overlap operator and for its favourable properties in addition to chirality (see below), while the similarity to $D_{\text{ovHF}}(m)$ is helpful for our algorithm to be discussed in Section 3.

Due to its perfect action background, D_{HF} is also endowed with a good scaling behaviour and approximate rotation symmetry, which are inherited by D_{ovHF} thanks to relation (2.4). That relation further provides a high level of locality for $D_{\text{ovHF}}^{(0)}$, since it deviates only little from the ultralocal operator D_{HF} . All these properties have been tested and confirmed extensively in the quenched re-weighted study of Ref. [34].

Let us reconsider here the level of *locality*, which is a key criterion in the comparison of different chiral lattice fermion formulations. We test it in the usual way [36], by applying $D_{\text{ovHF}}^{(0)}$ on a unit source η and measuring the decay of the function

$$f(r) = \max_x \left\{ D_{\text{ovHF},xy}^{(0)}(U) \eta_y \mid \sum_{\mu=1}^2 |x_\mu - y_\mu| = r \right\} , \quad \eta_y = \delta_{y0} \begin{pmatrix} 1 \\ 0 \end{pmatrix} . \quad (2.5)$$

We first consider the free fermion and demonstrate that this decay is clearly faster for the overlap-HF operator D_{ovHF} than for the Neuberger operator D_{N} , see Figure 2 on top. The plot below shows that the decay is still exponential for the configurations that we generated with dynamical fermions at $\beta = 5$, which confirms the locality of our Dirac operator. This assures that our lattice fermion formulation is conceptually on safe grounds. In the range that we studied, the mass has practically no influence on this decay rate. We observe that D_{ovHF} has a higher degree of locality than D_{N} , since D_{ovHF} at $\beta = 5$ is still clearly more local than even the free D_{N} : the decay for the free D_{ovHF} , $f(r) \propto \exp(-1.5 r)$, is reduced just slightly to $\exp(-1.45 r)$ by the gauge interaction, whereas D_{N} only decays as $\exp(-r)$ even in the absence of gauge fields.

This virtue also holds for the overlap-HF in quenched QCD [14, 37]: at $\beta = 6$ the exponent is increased by almost a factor of 2 compared to D_N , and the locality of overlap-HF is manifest down to $\beta = 5.6$. This enables the formulation of chiral fermions on coarser lattices than the use of D_N , which is of importance in view of QCD simulations at finite temperature. In that case, simulations are performed with a very small number N_t of lattice sites in the Euclidean time direction. Its extension is extremely expensive; the computational effort grows $\propto N_t^{12}$ [38]. The application of the D_{HF} — and in future also of D_{ovHF} — is therefore most promising in finite temperature QCD [39].

The scaling behaviour was found to be excellent for both, the HF and the overlap-HF, by considering dispersion relations in the free case and in the 2-flavour Schwinger model with quenched re-weighted configurations, which were generated at $\beta = 6$ [34]. The HF and the overlap-HF have an even better scaling behaviour than the (truncated) classically perfect action, which was constructed and tested for the Schwinger model in Ref. [20] (although that concept was actually designed for asymptotically free theories [40]). Another quenched re-weighted scaling test was added in Ref. [41].

Throughout this work we fix $\beta = 5$ and study the effects of varying the lattice size and the fermion mass. So we do not investigate explicitly the continuum extrapolation, since the scaling artifacts due to the finite lattice spacing turned out to be very small. This is illustrated by the dispersion relations of the “meson” masses shown in Figure 3: they follow the continuum behaviour up to quite large momenta, much further than the Wilson fermion or the Neuberger fermion [34]. Moreover scaling artifacts are expected to be negligible also based on the large plaquette values near 0.9, see Table 4. Hence the configurations are smooth, which corresponds to a fine lattice.

On the other hand, the issue of finite size effects is relevant here, and we will address it extensively in Sections 4 and 5. Figure 4 shows the correlation length $\xi = 1/M_\pi$ as a function of the fermion mass, as expected in infinite volume according to eq. (1.4). It reveals that significant finite size effects may occur for our smallest fermion masses and volumes. These effects can be very useful to investigate the distinction between topological sectors. In QCD they have been used to determine some of the Low Energy Constants by means of simulations in — or close to — the ϵ -regime [12–14, 16, 17, 42–44] and the δ -regime [45]. In our study the finite size effects are useful since they provide a suitable laboratory to probe methods of summing up observables measured separately in a few topological sectors. Section 5 presents pilot studies of such procedures, which might become relevant in lattice QCD.

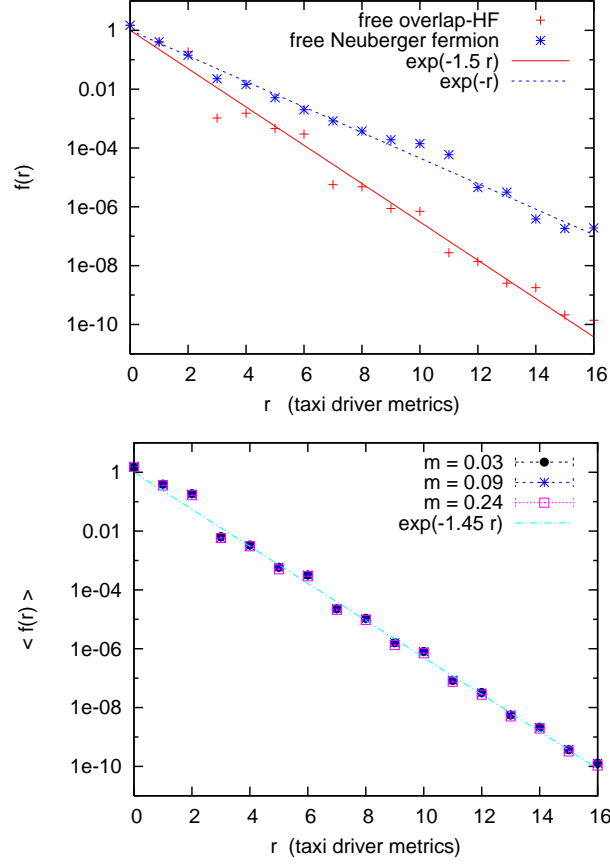


Figure 2: The locality of the overlap Dirac operators, tested by the decay of the function (2.5), against the taxi driver distance $r = |r_1| + |r_2|$. On top we compare our overlap-HF operator $D_{\text{ovHF}}^{(0)}$ to Neuberger's standard overlap operator D_N (with a Wilson kernel) in the free case. At $r = 3$ ($r = 7$), $f(r)$ is already suppressed by more than one (two) order(s) of magnitude for $D_{\text{ovHF}}^{(0)}$. The plot below shows the exponential decay of $\langle f(r) \rangle$ based on our overlap-HF simulations at $\beta = 5$. The gauge interaction reduces the decay rate just marginally, with hardly any dependence on the fermion mass m .

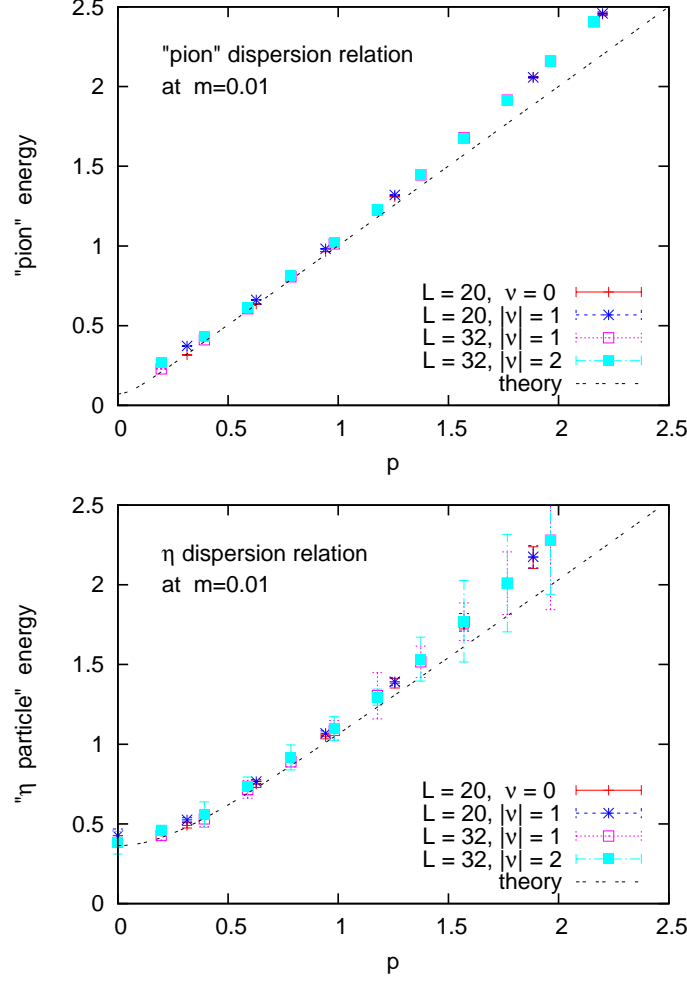


Figure 3: The dispersion relations for the “pion” and the “ η -particle” (isospin triplet and singlet), measured at fermion mass $m = 0.01$ at $L = 20$ and $L = 32$, in different topological sectors. Irrespective of the small differences, they follow in all cases very closely the theoretical curve in the continuum, given by eq. (1.4). Up to momentum $p \approx \pi/2$ lattice artifacts are tiny, which confirms an excellent scaling behaviour. This scaling quality is similar to the overlap-HF in our previous quenched re-weighted study at $\beta = 6$, but in that case the Wilson fermion and the Neuberger fermion show sizable scaling artifacts setting in at $p \approx 0.9$ [34].

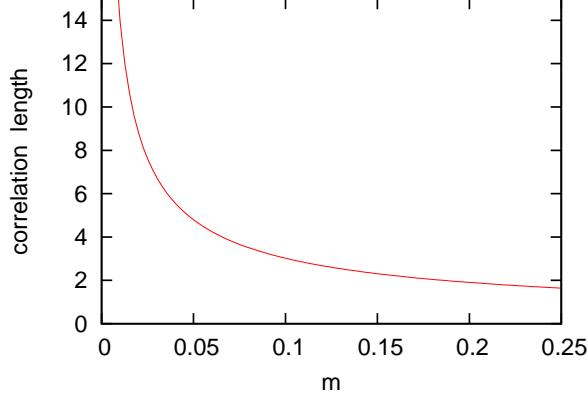


Figure 4: *The correlation length $\xi = 1/M_\pi$ (in infinite volume) as a function of the degenerate fermion mass m , according to eq. (1.4). For instance for our lightest fermion mass, $m = 0.01$, it amounts to $\xi \simeq 14$.*

3 Hybrid Monte Carlo with a preconditioned force

3.1 Algorithm

In order to simulate overlap-HFs dynamically, the standard Hybrid Monte Carlo (HMC) algorithm⁵ would use the fermionic force term

$$\bar{\psi} Q_{\text{ovHF}}^{-1} \left(Q_{\text{ovHF}}^{-1} \frac{\partial Q_{\text{ovHF}}}{\partial A_{x,\mu}} + \frac{\partial Q_{\text{ovHF}}}{\partial A_{x,\mu}} Q_{\text{ovHF}}^{-1} \right) Q_{\text{ovHF}}^{-1} \psi , \quad (3.1)$$

where $Q_{\text{ovHF}} = \gamma_5 D_{\text{ovHF}}$ is the Hermitian overlap-HF operator, and $A_{x,\mu}$ are the non-compact gauge link variables. However, this force term is computationally expensive. In particular in view of prospects for QCD we are going to explore a hopefully efficient alternative. In addition, the force (3.1) is conceptually problematic due to the discontinuous sign function $H_{\text{HF}}/\sqrt{H_{\text{HF}}^2}$ in Q_{ovHF} , see eq. (2.2). Under a continuous deformation of the configurations, the denominator vanishes at the transition between topological sectors. Here we refer to the proper definition of the topological charge by means of the fermionic index [28]

$$\nu = n_- - n_+ , \quad (3.2)$$

⁵The original work on the HMC algorithm is Ref. [46]; pedagogical descriptions can be found for instance in Refs. [47].

where n_+ (n_-) is the number of zero modes of $D_{\text{ovHF}}^{(0)}$ with positive (negative) chirality.⁶ Regarding the spectrum of H_{HF} , a topological transition means that an eigenvalue crosses 0, so its map by the overlap formula (2.2) flips between m and 2, *i.e.* it either appears as a zero mode of $D_{\text{ovHF}}^{(0)}$, or it is sent to the cutoff scale. Indeed the QCD simulations that have been performed with this HMC force hardly ever achieve topological transitions, see in particular Refs. [17, 48]; this issue is discussed in detail in Ref. [49]. We repeat that the same problem occurs also with other lattice Dirac operators for light dynamical fermions when the lattice becomes very fine [22]: the HMC history tends to get trapped in one topological sector.

Here we report on HMC simulations, which are again facilitated by the powerful property (2.4). Our algorithmic concept follows the HMC version, which was applied to improved staggered fermions of the HF-type in Ref. [50]. It used a sophisticated Dirac operator in the accept/reject step, but a simplified formulation for the force, which is quick to evaluate. In order to simulate the dynamical overlap-HF we render the force term continuous and computationally cheap by inserting only approximate overlap operators in the term (3.1). To be explicit, we apply an overlap-HF to a low precision ε' in the external factors Q_{ovHF}^{-1} , and we use H_{HF} instead of Q_{ovHF} in the derivatives (although this could be extended to a polynomial as well),⁷

$$\bar{\psi} Q_{\text{ovHF},\varepsilon'}^{-1} \left(Q_{\text{ovHF},\varepsilon'}^{-1} \frac{\partial H_{\text{HF}}}{\partial A_{x,\mu}} + \frac{\partial H_{\text{HF}}}{\partial A_{x,\mu}} Q_{\text{ovHF},\varepsilon'}^{-1} \right) Q_{\text{ovHF},\varepsilon'}^{-1} \psi . \quad (3.3)$$

For the integration we applied the Sexton-Weingarten scheme [51] with a partial $(\delta\tau)^3$ correction (where $\delta\tau$ is the step size). The time scales for the fermionic vs. gauge force had the ratio of 1:5, but we did not observe much sensitivity to this ratio.

The Metropolis accept/reject step is performed with the high precision overlap operator $D_{\text{ovHF},\varepsilon}$. Hence the deviations in the force are corrected, and the point to worry about is just the acceptance rate. The complete simplification, which reduces $Q_{\text{ovHF},\varepsilon'}$ to $\gamma_5 D_{\text{HF}}$, was considered in Ref. [52], which found a decreasing acceptance rate for increasing volume; that study was based on the Scaling Optimised Hypercube Fermion (SO-HF) of Ref. [34]. However, in this respect it turns out to be highly profitable — and still cheap — to correct the external factors to a modest precision. We

⁶We fix the sign of the index such that it matches the continuum gauge formulation of the topological charge, $\int d^2x \epsilon_{12} F_{12}$. However, in all considerations of this work only $|\nu|$ matters.

⁷The simplified force that we are using is not only computationally cheaper, but it is also expected to be helpful to achieve at least a few topological transitions. Hence it might not even be favourable to extend H_{HF} in eq. (3.3) to a polynomial, which would move the force formulation closer to the dangerous sign function.

m	number of configurations				topological transitions
	$\nu = 0$	$ \nu = 1$	$ \nu = 2$	total	
0.01	2428	307		2735	7
0.03	1070	508		1578	2
0.06	741	660		1401	7
0.09	919	587	1	1507	7
0.12	664	501	248	1413	8
0.18	791	563	50	1404	15
0.24	576	978	56	1637	17

Table 2: *Our statistics of configurations at $L = 16$ and seven fermion masses m . The HMC trajectory lengths ℓ are given in Table 4. In all cases they consist of 20 integration steps ($\delta\tau = \ell/20$). The measurements are separated by at least 200 trajectories. For $m = 0.01$ this separation was enlarged to 600 trajectories for a better decorrelation. As a generic property of dynamical overlap fermion simulations, topological transitions are rare, as we see in particular for our lightest fermion masses.*

chose the algorithmic parameters for the (absolute) precisions as

$$\varepsilon' = 0.005 \quad (\text{force term}) , \quad \varepsilon = 10^{-16} \quad (\text{Metropolis step}) , \quad (3.4)$$

which increases the acceptance rate by an order of magnitude compared to the simple use of H_{HF} throughout the force term. The force we obtain in this way is not based on Hamiltonian dynamics, but the way it deviates from it (by proceeding from $\gamma_5 D_{\text{HF}}$ to $Q_{\text{ovHF},\varepsilon'}$) does maintain the property of area conservation in phase space.

3.2 Statistics

With this algorithm, we performed production runs at $\beta = 5$ on $L \times L$ lattices of the sizes $L = 16, 20, 24, 28$ and 32 . On the 16×16 lattice we collected statistics at seven fermion masses in the range $m = 0.01 \dots 0.24$ in distinct topological sectors, as displayed in Table 2. At our lightest mass, $m = 0.01$, we performed additional simulations on larger lattices of size $L = 20 \dots 32$, plus runs at $m = 0.06$, $L = 32$, see Table 3.

Since the force term (3.3) tends to push the trajectory a bit off the hyper-surface of constant energy, we kept the trajectory length ℓ (between the Metropolis steps) short. At $L = 16$, $m \leq 0.18$, we chose $\ell = 1/8$, which is divided into 20 integration steps ($\delta\tau = 0.00625$). This was a compromise in view of precision and dynamics between the trajectory end-points. On the larger lattices the trajectory length ℓ was further reduced, see Table

L	m	number of configurations				total
		$ \nu = 0$	$ \nu = 1$	$ \nu = 2$	$ \nu = 3$	
20	0.01	435	304			739
24	0.01			278	273	551
28	0.01		240		180	420
32	0.01	138	98	82		318
32	0.06	91	293			384

Table 3: *Our statistics for the lattice sizes $L = 20 \dots 32$ at fermion masses $m = 0.01$ and 0.06 . The trajectory length ℓ was reduced for increasing L , see Table 4, while the integration step was always fixed as $\delta\tau = \ell/20$. After thermalisation, the configurations are separated by at least 200 trajectories. We show our statistics in the topological sectors $|\nu| = 0 \dots 3$. In particular at $m = 0.01$ topological transitions were very rare, so we captured various sectors by a multitude of “hot starts”.*

4.⁸

The configurations used for the measurements were separated by at least 200 trajectories. Still the autocorrelation with respect to the observables in Sections 4 and 5 is not always negligible, see Table 5. In particular some problems show up for $L > 20$ and higher topological charges, which suggests that an application of this algorithmic approach to QCD might require further refinements. Here autocorrelations were taken into account by a jackknife analysis of the measured data. That method was used for the error calculations throughout this work; we probed a variety of bin sizes and took the maximal error in each case.

3.3 Reversibility, acceptance rate and computational effort

Reversibility — to a good precision — is a requirement of the HMC algorithm. The possible danger for this crucial property could be an instability in the molecular dynamics trajectory due to directions with positive Lyapunov exponents, such that certain deviations from the exact trajectory are amplified exponentially [53].

To test if we are confronted with this problem, we moved forth and back with a variable number of steps, and measured the (absolute) modification of the gauge action, $|\Delta S_G|$. As examples, Figure 5 (on top) shows our results for the reversibility precision at $L = 16$, $\delta\tau = 0.00625$, for the

⁸At a few points in the HMC histories, where the algorithm run into convergence problems, we temporarily reduced ℓ below the trajectory length given in Table 4, always maintaining the dissection into $\delta\tau = \ell/20$.

masses $m = 0.03$, 0.12 and 0.24 . The precision is satisfactory in all cases. It still improves significantly for increasing mass, as we also observe for $\delta\tau = 0.005$, see Figure 5 (below). Our results do not indicate the presence of any positive Lyapunov exponent.

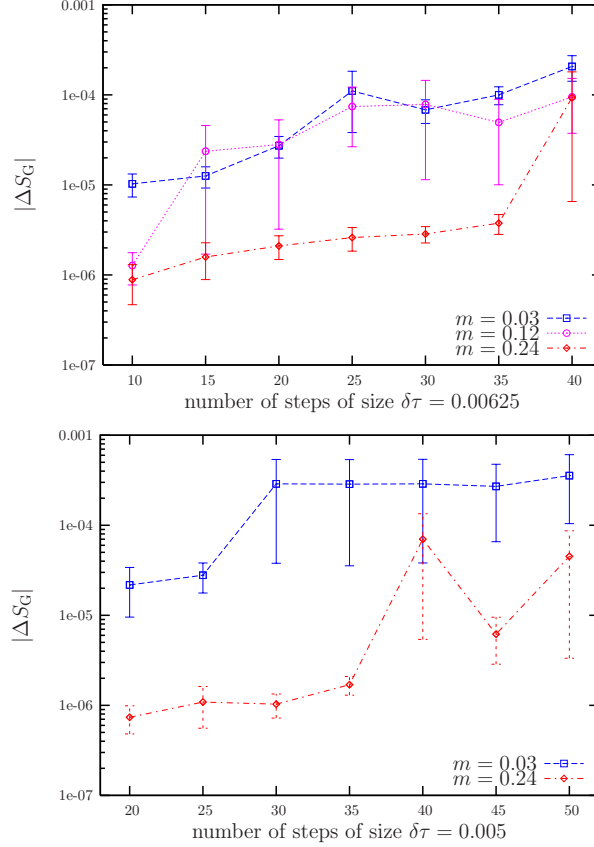


Figure 5: *The reversibility precision with respect to the gauge action S_G for a variable number of steps of length $\delta\tau = 0.00625$ (on top) and $\delta\tau = 0.005$ (below), both on a 16×16 lattice at $\beta = 5$. We show results for very different masses. There is no indication for any positive Lyapunov exponent. The precision improves as we increase m , but it is satisfactory in all cases.*

Being confident that our algorithm is safe, we now proceed to the question of its efficiency. The plots in Figure 6 show the *acceptance rates* in the Metropolis step.⁹ In some sectors they were somewhat modest for the parameters chosen here, which is related to the aforementioned cases of rather long autocorrelation times.

⁹We evaluated the acceptance rate by considering the acceptance probability in each Metropolis step, regardless of the actual accept/reject decision. This is statistically more conclusive than just counting the acceptance ratio.

Figure 7 displays the number of *Conjugate Gradient iterations* that was required per trajectory, specifically in the evaluation of D_{ovHF} (upper plots) and in total (lower plots). Table 4 summarises the acceptance rates, as well as the number of Conjugate Gradient steps in the evaluation of the overlap operator and in total. We add the plaquette value to characterise the smoothness of the configurations; this serves as a point of orientation for comparison with other models in lattice gauge theory.

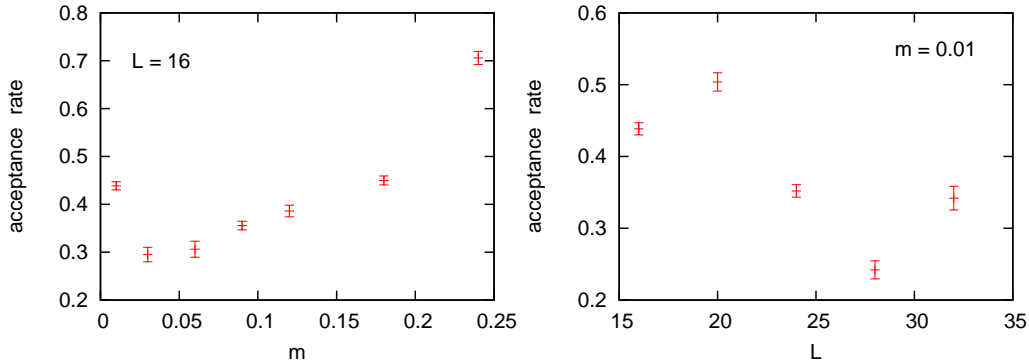


Figure 6: *The Metropolis acceptance rate on the $L = 16$ lattice at seven different masses (on the left), and at $m = 0.01$ on five lattice sizes (on the right). Note that the trajectory length varies, as specified in Table 4.*

As usual, the simulation becomes faster when we proceed from light to moderate fermion mass. However, the number of Conjugate Gradient iterations rises only mildly as we approach the chiral limit, even down to very light masses. The reason is that finite size effects prevent the non-zero eigenvalues from becoming really tiny (this virtue is obviously reduced if the volume increases). The low-lying non-zero eigenvalues will be discussed in detail in the next section.

4 The Dirac spectrum

In this section we discuss our results for the eigenvalues of the Dirac operator $D_{\text{ovHF}}^{(0)}$ in eq. (2.2), after stereographic projection (a Möbius transform) onto the half-line \mathbb{R}_+ ,

$$\lambda_i \rightarrow \left| \frac{\lambda_i}{1 - \lambda_i/2} \right|. \quad (4.1)$$

4.1 Unfolded level spacing distribution

We first consider the full spectra and the resulting unfolded level spacing distribution. This distribution is obtained as follows: one first numerates

L	m	ℓ	acceptance rate	number of CG iterations in D_{ovHF}	total	plaquette value
16	0.01	0.125	0.439(8)	97.2(1)	4529(4)	0.8971(2)
16	0.03	0.125	0.295(15)	94.2(1)	4419(5)	0.8965(4)
16	0.06	0.125	0.306(17)	93.9(1)	4405(4)	0.8974(4)
16	0.09	0.125	0.355(9)	91.4(1)	4312(2)	0.8963(2)
16	0.12	0.125	0.386(12)	89.6(1)	4244(3)	0.8961(3)
16	0.18	0.125	0.450(9)	82.7(1)	3966(2)	0.8965(2)
16	0.24	0.0625	0.706(13)	76.5(1)	3708(3)	0.8947(4)
20	0.01	0.0625	0.504(13)	128.7(2)	5961(6)	0.8972(3)
24	0.01	0.05	0.352(9)	149.9(6)	7129(27)	0.8969(5)
28	0.01	0.04	0.242(13)	191.9(2)	9152(17)	0.8972(5)
32	0.01	0.03	0.342(16)	224.9(5)	10432(18)	0.8968(5)
32	0.06	0.03	0.619(10)	199.0(2)	9546(8)	0.8971(3)

Table 4: *The characteristic indicators for the performance of the preconditioned HMC algorithm: first we give the acceptance rate in the Metropolis step at the end of each trajectory of length ℓ . The accept/reject step uses D_{ovHF} to machine precision (see eq. (3.4)). We add the number of Conjugate Gradient iterations needed to evaluate the operator D_{ovHF} and in total. Finally we quantify the smoothness of the configurations by the mean plaquette value.*

L	m	$ \nu $	plaquette	Dirac eigenvalue λ_1	chiral condensate Σ
16	0.01	0	0.6	0.7	1.1
16	0.01	1	0.7	0.5	0.8
16	0.03	0	0.6	1.2	1.2
16	0.03	1	0.5	1.0	1.1
16	0.06	0	0.6	1.2	1.2
16	0.06	1	0.7	0.9	0.9
16	0.09	0	< 0.5	1.2	1.2
16	0.09	1	< 0.5	0.9	1.0
16	0.12	0	< 0.5	1.5	1.3
16	0.12	1	0.5	0.9	0.9
16	0.12	2	0.5	0.8	0.9
16	0.18	0	< 0.5	1.1	0.9
16	0.18	1	0.6	0.7	0.7
16	0.18	2	< 0.5	0.6	0.6
16	0.24	0	< 0.5	1.1	1.1
16	0.24	1	< 0.5	0.9	0.7
16	0.24	2	< 0.5	0.5	< 0.5
20	0.01	0	< 0.5	1.3	0.9
20	0.01	1	< 0.5	1.2	1.1
24	0.01	2	< 0.5	2.5	2.5
24	0.01	3	0.6	2.8	2.4
28	0.01	1	0.5	2.7	1.7
28	0.01	3	0.5	4.5	5.0
32	0.01	0	< 0.5	1.3	1.2
32	0.01	1	< 0.5	1.8	1.6
32	0.01	2	1.3	1.7	1.9
32	0.06	0	< 0.5	0.9	0.8
32	0.06	1	< 0.5	1.9	2.7

Table 5: *The integrated autocorrelation times $\tau_{\text{int}} = \frac{1}{2} + \sum_{\tau \geq 1} C(\tau)$ (where $C(\tau)$ is the autocorrelation function) over a total trajectory length 25, for the mean plaquette value, the leading non-zero Dirac eigenvalue λ_1 (relevant in Section 4), and the chiral condensate Σ (relevant in Section 5).*

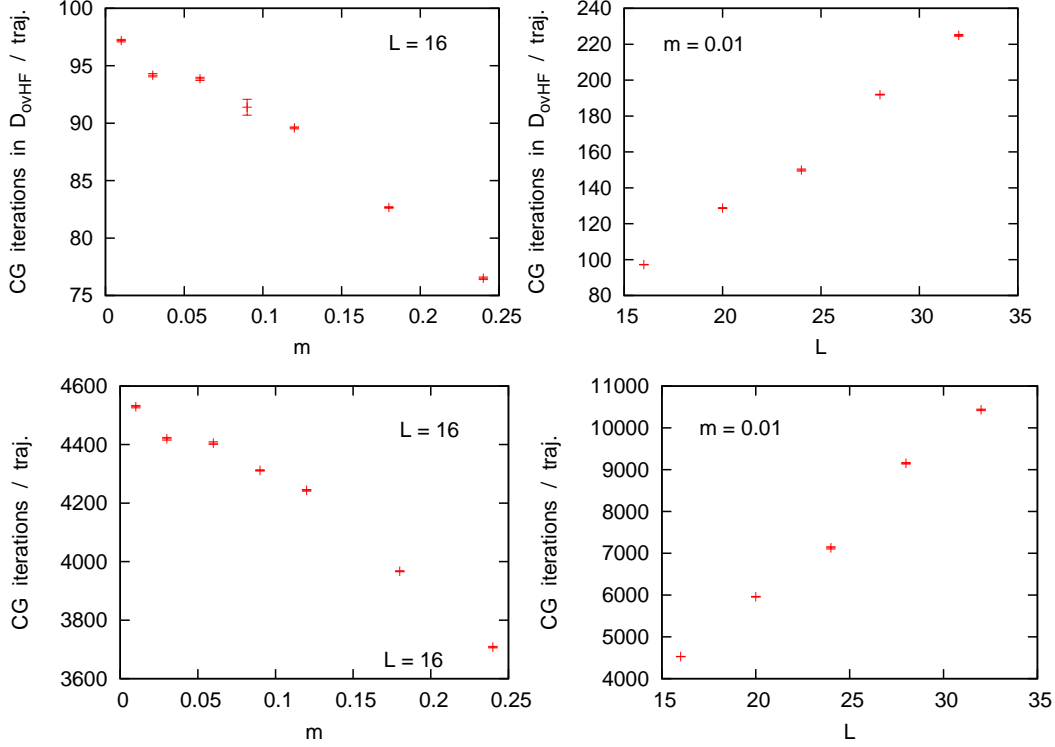


Figure 7: The number of Conjugate Gradient iterations per trajectory in D_{0vHF} (upper plots), and including all operations (lower plots). We show results at $L = 16$ and various masses (plots on the left), and at $m = 0.01$ on various lattice sizes (plots on the right).

the eigenvalues of single configurations in ascending order, λ_i (here we omit the eigenvalues with negative imaginary parts before the mapping (4.1)). Next we put all eigenvalues in a set of configurations together and numerate them again. Now we consider pairs of eigenvalues λ_i, λ_{i+1} (of the same configuration), and count by how many ordinal numbers they differ in the overall order. This difference — divided by the number of configurations involved — is the *unfolded level spacing*.

Random Matrix Theory (RMT) predicts three shapes for the statistical distribution of these level spacings. They refer to the three possible patterns of spontaneous chiral flavour symmetry breaking (for N_f flavours),

$$\begin{aligned}
SU(2N_f) &\rightarrow SO(2N_f) && \text{orthogonal} \\
SU(N_f) \otimes SU(N_f) &\rightarrow SU(N_f) && \text{unitary} \\
SU(2N_f) &\rightarrow Sp(2N_f) && \text{symplectic} .
\end{aligned} \tag{4.2}$$

At least in 4d Yang-Mills theory with chiral fermions, this set of patterns

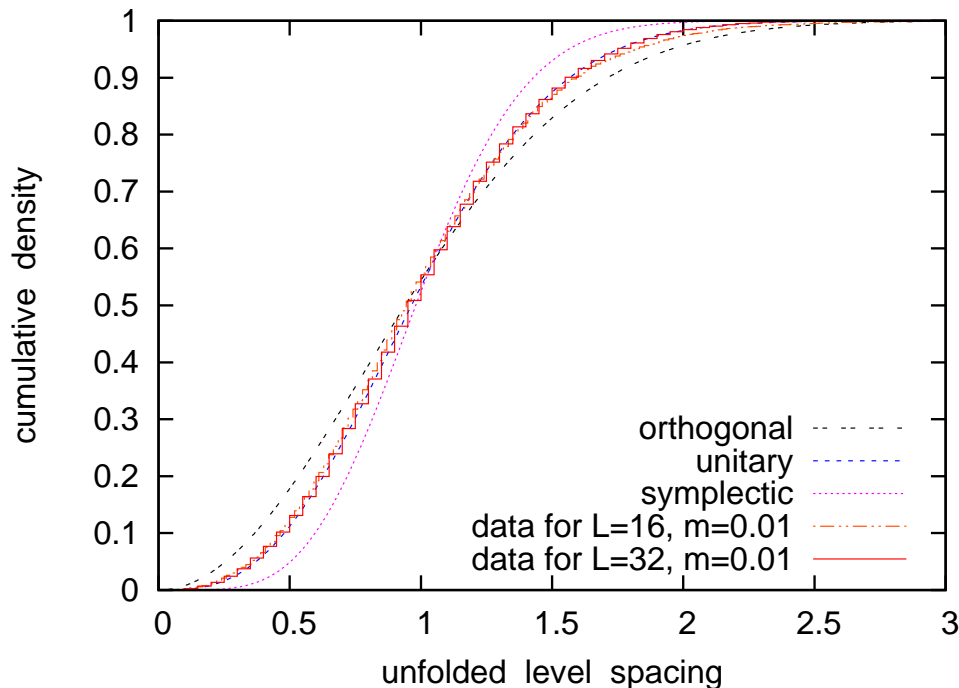


Figure 8: *The cumulative density of the unfolded level spacing distribution. We show the curves corresponding to the RMT prediction for the orthogonal, the unitary and the symplectic ensemble, and confront them with our simulation data (for our lightest fermion mass, $m = 0.01$). We clearly observe agreement with the RMT formula for the unitary ensemble. For $L = 16$ there is still a slight deviation for level spacings $\gtrsim 1.5$. As we increase the size to $L = 32$, even this deviation practically disappears, i.e. the agreement becomes very precise.*

is complete [54].¹⁰ They correspond to the real, complex and pseudo-real fermion representation of the gauge group. (In the real and pseudo-real case, fermion and anti-fermion representations are equivalent, hence the unbroken symmetry is enlarged to $SU(2N_f)$.) Ref. [56] elaborated the corresponding formulae for the unfolded level spacing distributions. For lattice QCD (with chiral quarks) the prediction of the unitary ensemble has been confirmed [12, 57], but the case of the 2-flavour Schwinger model is theoretically less clear, because there is no spontaneous breaking of the chiral flavour symmetry.

Our results (for $m = 0.01$, as an example) are shown in Figure 8. We

¹⁰An overview of the conceivable types of chiral symmetry breaking with an isomorphic representation by non-unitary groups is given in Ref. [55].

L	m	$\langle \lambda_{1, \nu=0} \rangle$	$\langle \lambda_{1, \nu =1} \rangle$	$\langle \lambda_{1, \nu =2} \rangle$	$\langle \lambda_{1, \nu =3} \rangle$
16	0.01	0.1328(6)	0.175(2)		
16	0.03	0.130(2)	0.173(2)		
16	0.06	0.125(2)	0.173(1)		
16	0.09	0.115(2)	0.172(2)		
16	0.12	0.108(2)	0.166(2)	0.216(3)	
16	0.18	0.108(2)	0.166(2)	0.221(4)	
16	0.24	0.109(3)	0.163(2)	0.215(4)	
20	0.01	0.102(2)	0.127(2)		
24	0.01			0.125(4)	0.148(6)
28	0.01		0.082(3)		0.120(5)
32	0.01	0.057(3)	0.076(3)	0.084(3)	
32	0.06	0.030(3)	0.054(3)		

Table 6: *The lowest non-zero eigenvalue of $D_{\text{ovHF}}^{(0)}$ (after the stereographic projection (4.1)) for different masses and lattice sizes, in distinct topological sectors.*

see very clear agreement with the RMT formula for the unitary ensemble. The tiny deviation that we observe for $L = 16$ is a finite size effect, which is manifestly suppressed as we enlarge the lattice size to $L = 32$.

4.2 The microscopic Dirac spectrum

We now focus on the leading non-zero eigenvalue λ_1 , based on the statistics presented in Tables 2 and 3. The results for $\langle \lambda_1 \rangle$ are given in Table 6. We mentioned before that chiral RMT has been worked out for the case of a finite condensate $\Sigma(m \rightarrow 0)$ [10, 11], with successful applications in the ϵ -regime of QCD. This is not the situation we are dealing with; here Σ vanishes in the chiral limit, as eq. (1.3) shows. The situation is qualitatively similar for fermions interacting through Yang-Mills gauge fields above the critical temperature of the chiral phase transition. Also there the understanding of the Dirac spectra is controversial; for numerical studies and conjectures we refer to Refs. [58, 59].

In infinite volume, $V \rightarrow \infty$, the chiral condensate is given by the Dirac spectrum as

$$\Sigma = \int d\lambda \frac{\rho(\lambda)}{\lambda + m} \quad (\rho : \text{eigenvalue density}) . \quad (4.3)$$

Along with the prediction quoted in Section 1, $\Sigma \propto m^{1/3}$, this suggests [19]

$$\rho(\lambda \gtrsim 0) \propto \lambda^{1/3} , \quad (4.4)$$

in contrast to the Banks-Casher plateau [9] that one obtains in the standard setting (with $\Sigma(m \rightarrow 0) \neq 0$). In that case, the density for the re-scaled small eigenvalues $\lambda_i \Sigma V$ is scale-invariant (at fixed $m \Sigma V$) [60]. In our case, the generic relation $\langle \lambda_i \rangle \propto [V \rho(\lambda \gtrsim 0)]^{-1}$ suggests that the parameter

$$\zeta_i = \lambda_i V^{3/4} W_\zeta \quad (\text{for small } \lambda_i ; V = L^2) \quad (4.5)$$

should adopt this rôle, at fixed $\mu_\zeta = m V^{3/4} W_\zeta$ — or simply at small m . W_ζ is a constant of dimension $[\text{mass}]^{1/2}$, which is (in this context) analogous to Σ in the standard setting.

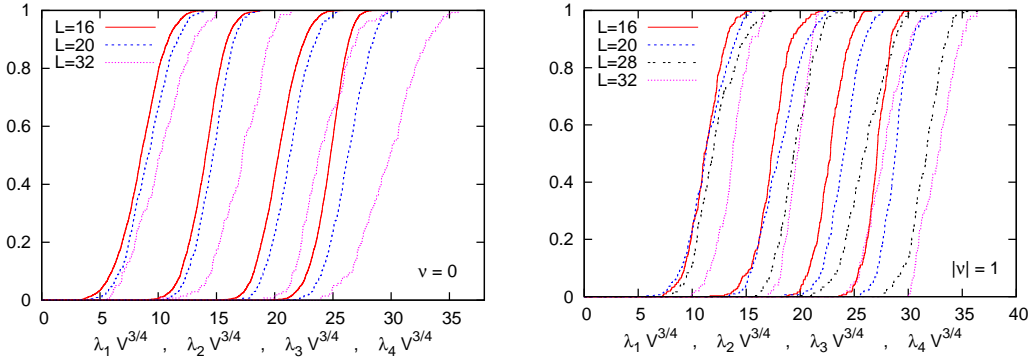


Figure 9: *Cumulative densities of $\lambda_i V^{3/4} \propto \zeta_i$, for $i = 1 \dots 4$, at mass $m = 0.01$ and topological charge $\nu = 0$ (on the left) resp. $|\nu| = 1$ (on the right). We see that ζ_i deviates from scale-invariance.*

Hence we probed the corresponding finite-size scaling, but it is *not* confirmed. This is illustrated in Figure 9 for our lightest fermion mass, $m = 0.01$, in the sectors of topological charge $\nu = 0$ and $|\nu| = 1$. As a quantitative measure, the integrated variance is given — and compared to better approaches — in Table 7. Note, however, that the derivation of relation (4.4) may be invalidated by inserting an explicitly mass-dependent spectral density, $\rho(\lambda, m)$, in eq. (4.3).

Next we consider another scenario, with a reduced exponent of V in the re-scaling factor. Now we assume the scale-invariant variable to be $Z_i = \lambda_i V^{2/3} W_Z$ (W_Z of dimension $[\text{mass}]^{1/3}$). This scenario is motivated by the fact that it belongs to a theoretically well explored universality class: it corresponds to $\rho(\lambda \gtrsim 0) \propto \lambda^{1/2}$, which is the spectral density obtained by RMT in the *Gaussian approximation*. There is a precise prediction for the corresponding spectral density in terms of Airy functions [58],

$$\rho_{\text{Airy}}(Z) \propto Z[\text{Ai}(-Z)]^2 + [\text{Ai}'(-Z)]^2 \quad (\sim \sqrt{Z}/\pi \text{ at } Z \gg 1) . \quad (4.6)$$

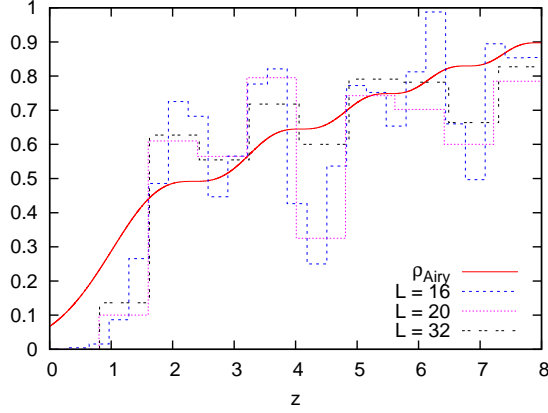


Figure 10: *Eigenvalue histograms for $Z_1 \propto \lambda_1 V^{2/3}$, at $m = 0.01$, $\nu = 0$ compared to the spectral density ρ_{Airy} in eq. (4.6), which RMT predicts in the Gaussian approximation. There is no convincing support for this scenario.*

Figure 10 compares the Airy function density (4.6) to the histograms that we obtained in various volumes at $m = 0.01$ and $\nu = 0$. Our data exhibit a far more marked wiggle structure, hence the agreement is not really convincing.

The finite size scaling quality of Z_1 is also captured in Table 7. It is significantly better than the one of ζ_1 , but still not fully satisfactory.

Let us finally proceed to the most successful approach, which was identified empirically. It turns out that our data are in excellent agreement with a scale-invariant parameter

$$z_i = \lambda_i V^{5/8} W_z \quad (W_z : \text{constant of dimension } [\text{mass}]^{1/4}) , \quad (4.7)$$

which implies a microscopic spectral density $\rho(\lambda) \propto \lambda^{3/5}$. The scale invariance of $z_1 \dots z_4$ is illustrated in Figure 11, again for our lightest fermion mass, $m = 0.01$, in the sectors of topological charge $\nu = 0$ and $|\nu| = 1$, which can be compared directly to Figures 9. A quantitative confrontation with the previous two ansätze is included in Table 7.

We also tested the behaviour if the re-scaled mass is kept approximately constant, as an alternative to just keeping m small. In Figure 12 we compare $\langle \zeta_i \rangle$ for different lattice sizes, $L = 16$ and 32 , again in the sectors $|\nu| = 0$ and 1 , for $\mu_\zeta \approx \text{const.}$ We add the corresponding test with $\langle z_i \rangle$ and $\mu_z = m V^{5/8} W_z \approx \text{const.}$, which reveals again a clearly superior finite size scaling.

Our data favour this last scenario unambiguously. A hint for a possible explanation can be found in Ref. [5], which introduced the dimensionless

index $ \nu $	0			1		
power p	3/4	2/3	5/8	3/4	2/3	5/8
Var_{int}	1.812	0.266	0.026	2.078	0.258	0.066
$\text{Var}_{\text{int}}^{(n)}$	0.159	0.036	0.007	0.204	0.055	0.019

Table 7: A measure for the agreement between the cumulative densities of the re-scaled eigenvalues $s_i = \lambda_i V^p$, at $m = 0.01$ and $|\nu| = 0, 1$. We show $\text{Var}_{\text{int}} = \sum_{i=1}^4 \int ds_i [\sum_{k=1}^{\max} (\rho_{L_k}(s_i) - \rho_m(s_i))^2] / (\max - 1)$, the integrated variance, where the sum over k includes $L_k = 16, 20, 32$ at $\nu = 0$ ($\max = 3$), and $L_k = 16, 20, 28, 32$ at $|\nu| = 1$ ($\max = 4$). $\rho_m(s_i)$ is the mean value over the volumes involved. The quantity $\text{Var}_{\text{int}}^{(n)}$ is normalised by dividing through the relevant interval in s , where $0.01 < \rho_m(s) < 0.99$. We confirm that the power $p = 5/8$ yields by far the least variance, i.e. the best agreement.

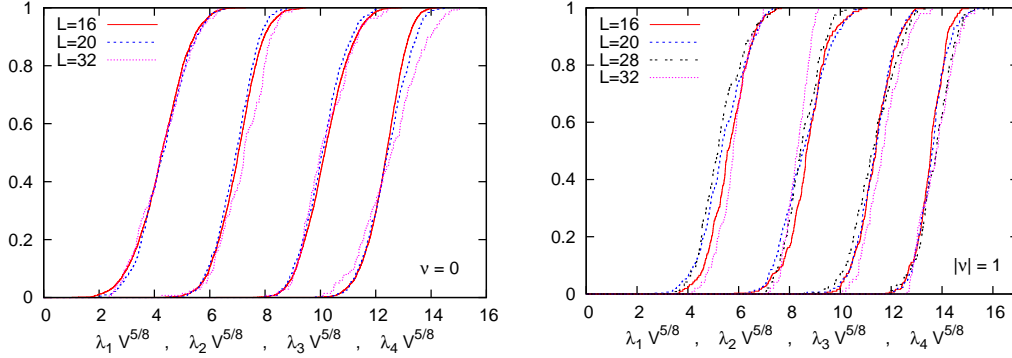


Figure 11: Cumulative densities of $\lambda_i V^{5/8} \propto z_i$, for $i = 1 \dots 4$, at mass $m = 0.01$ and topological charge $\nu = 0$ (on the left) resp. $|\nu| = 1$ (on the right). In contrast to ζ_i and Z_i , the variable z_i is scale-invariant to an impressive precision.

parameter

$$l := \sqrt{2}mL^{3/2}/(\beta\pi)^{1/4} \quad (4.8)$$

to distinguish different regimes. The aforementioned behaviour $\Sigma \propto m^{1/3}$ is expected for $l \gg 1$, whereas $l \ll 1 \ll 2L/\sqrt{\pi\beta}$ implies $\Sigma \propto mL$. For $m = 0.01$ we are in an *intermediate regime*, $l = 0.5 \dots 1.3$ (and $2L/\sqrt{\pi\beta} = 8.1 \dots 16.2$), which renders our exponent in $\Sigma \propto m^{3/5}$ plausible.

However, a precise explanation for this behaviour remains to be worked out. In particular in the framework of RMT — extended to this extraordinary setting — this might be feasible, but it is far from trivial [61].

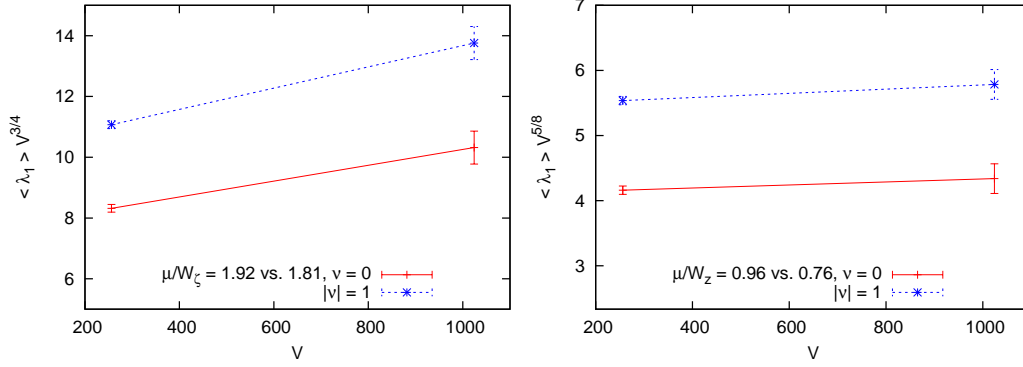


Figure 12: *Finite size scaling for $\langle \zeta_1 \rangle$ at $\mu_\zeta \propto mV^{3/4} \approx \text{const.}$ (left) and $\langle z_1 \rangle$ at $\mu_z \propto mV^{5/8} \approx \text{const.}$ (right). These plots confirm again that z_1 performs much better as a scale-invariant variable.*

4.3 Eigenvalues in the bulk of the Dirac spectrum

At last we take a look at λ_{10} as one of the bulk eigenvalues, and we find an optimal finite size scaling for $\lambda_{10} L^{1.15}$, see Figure 13 (left). The plot on the right shows that this factor works well also for the re-scaled full cumulative density (including all eigenvalues up to the considered value). Based on the fact that the spectral cutoff $\lambda_{\text{max}} = 2$ is fixed in any volume,

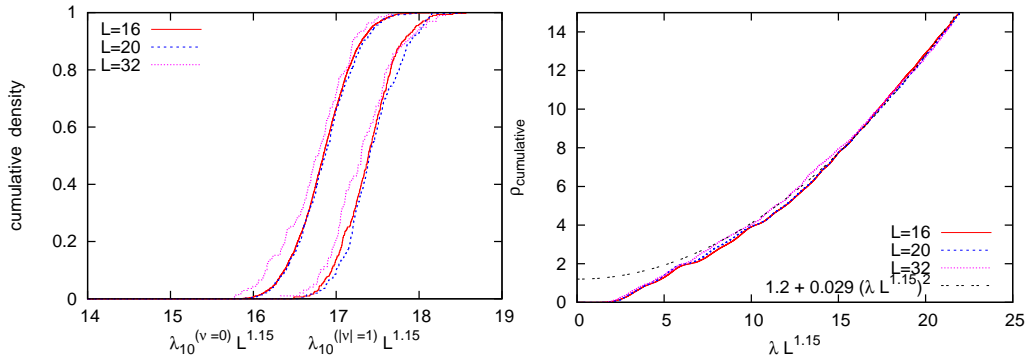


Figure 13: *For λ_{10} , a low-lying bulk eigenvalue, the scaling factor is shifted to $L^{1.15}$. The re-scaled full spectral cumulative densities in different volumes (for $m = 0.01$, $\nu = 0$) agree well, and turn into the bulk behaviour $\rho(\lambda) \propto \lambda$ (resp. $\rho_{\text{cumulative}}(\lambda) \propto \lambda^2$), which is expected in $d = 2$.*

it is now tempting to speculate that the volume factor for a good finite size scaling gradually decreases from $V^{3/5} \dots V^0$. However, considering eigenvalues above the regime shown in Figure 13, but below the cutoff regime, we could not find any consistent scaling factor. Indeed there is no compelling reason for such a factor to exist.

5 Topological summation and susceptibility

The chiral condensate Σ can be measured using the complete Dirac spectrum,

$$\Sigma = \frac{1}{V} \sum_i \frac{1}{\lambda_i + m} , \quad (5.1)$$

where we still refer to the eigenvalues λ_i after the projection (4.1). Here we do not need any assumptions from RMT or the ϵ -regime. We want to investigate the link to the analytical formula for $\Sigma(m)$ in eq. (1.3).

However, since there are only few topological transitions in the HMC history (cf. Table 2), we can only measure

$$\Sigma_{|\nu|} = -\langle \bar{\psi} \psi \rangle_{|\nu|} , \quad (5.2)$$

i.e. the chiral condensate in separate topological sectors. Hence an appropriate summation has to be performed. This challenge is generic for HMC simulations with dynamical light fermions on fine lattices, so it is relevant — in particular in view of QCD — to explore such topological summations. Here we encounter an interesting test bed to probe various methods for this purpose.

For very light fermions, the dominant contribution to $\Sigma_{\nu \neq 0}$ is due to the zero modes. Hence a suitable notation is

$$\Sigma_\nu = \frac{|\nu|}{mV} + \varepsilon_{|\nu|} , \quad \varepsilon_0 > \varepsilon_1 > \varepsilon_2 > \dots > 0 . \quad (5.3)$$

The inequalities at the end correspond to a general property of stochastic Hermitian matrices (such as $\gamma_3 D_{\text{ovHF}}$): the presence of zero modes pushes the small non-zero eigenvalues to higher (absolute) values.

Our results for the direct measurement of Σ_ν are given in Table 8. The hierarchy anticipated in relation (5.3) is consistently confirmed. In addition we observe the inequality

$$\varepsilon_{|\nu|}(V_1) > \varepsilon_{|\nu|}(V_2) \quad \text{if} \quad V_1 > V_2 \quad (5.4)$$

to hold. If the volume is enlarged, the non-zero eigenvalues reach out to smaller values. We see that this effect supersedes the pre-factor $1/V$ in eq. (5.1), so that $\varepsilon_{|\nu|}$ increases. The validity of inequalities (5.3), (5.4) is illustrated in Figure 14. Moreover, we recognise a smooth mass and volume dependence of the terms $\varepsilon_{|\nu|}$.

L	m	$\langle \Sigma_{\nu=0} \rangle$ $\langle \varepsilon_{\nu=0} \rangle$	$\langle \Sigma_{ \nu =1} \rangle$ $\langle \varepsilon_{ \nu =1} \rangle$	$\langle \Sigma_{ \nu =2} \rangle$ $\langle \varepsilon_{ \nu =2} \rangle$	$\langle \Sigma_{ \nu =3} \rangle$ $\langle \varepsilon_{ \nu =3} \rangle$	$\langle \Sigma_{ \nu =4} \rangle$ $\langle \varepsilon_{ \nu =4} \rangle$
16	0.01	0.01273(8) 0.01273(8)	0.39968(5) 0.00905(5)			
16	0.03	0.0374(4) 0.0374(4)	0.1573(2) 0.0271(2)			
16	0.06	0.0713(8) 0.0713(8)	0.1174(2) 0.0523(2)			
16	0.09	0.0985(8) 0.0985(8)	0.1182(3) 0.0748(3)			
16	0.12	0.1174(6) 0.1174(6)	0.1275(4) 0.0949(4)	0.1468(4) 0.0817(4)		
16	0.18	0.1434(3) 0.1434(3)	0.1469(3) 0.1252(3)	0.1548(4) 0.1114(4)		
16	0.24	0.1633(4) 0.1633(4)	0.1652(2) 0.1489(2)	0.1697(4) 0.1371(4)	0.1758(9) 0.1270(9)	0.1841(7) 0.1190(7)
20	0.01	0.0141(3) 0.0141(3)	0.2608(3) 0.0108(3)			
24	0.01			0.3572(2) 0.0100(2)	0.5296(2) 0.0088(2)	
28	0.01		0.1408(2) 0.0132(2)		0.3923(2) 0.0096(2)	
32	0.01	0.0181(5) 0.0181(5)	0.1112(2) 0.0135(2)	0.2073(4) 0.0120(4)		
32	0.06	0.0883(7) 0.0883(7)	0.093(1) 0.077(1)			

Table 8: *Results for the directly measured chiral condensate at different masses and lattice sizes, in distinct topological sectors. We observe full agreement with inequalities (5.3) and (5.4). As m increases at fixed L , the dominant rôle of the zero mode contributions to $\Sigma_{\nu \neq 0}$ is diminished. As L increases at fixed m , however, $\varepsilon_{|\nu|}$ is enhanced.*

5.1 Gaussian evaluation of the topological susceptibility

In this method we assume a Gaussian distribution of the topological charges, so that Σ can be written as

$$\Sigma = \sum_{\nu=-\infty}^{\infty} p(|\nu|) \Sigma_{|\nu|}, \quad p(|\nu|) = \frac{\exp\left(-\frac{\nu^2}{2V\chi_t}\right)}{\sum_{\nu=-\infty}^{\infty} \exp\left(-\frac{\nu^2}{2V\chi_t}\right)}, \quad (5.5)$$

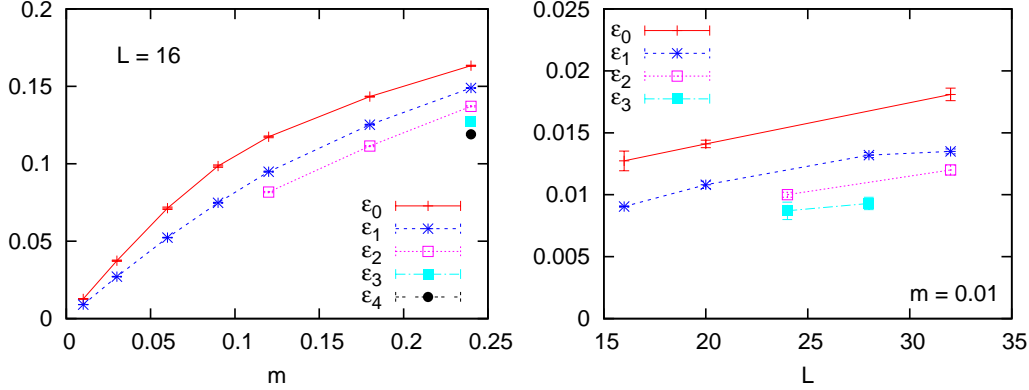


Figure 14: The terms $\varepsilon_{|\nu|}$ introduced in eq. (5.3), which represent the contribution of the non-zero modes to the chiral condensate in a fixed topological sector. These plots reveal a smooth and monotonous dependence on the fermion mass (on the left, at $L = 16$) and on the volume (on the right, at $m = 0.01$).

where χ_t is the topological susceptibility. At least in QCD the charge distribution is indeed Gaussian to a good approximation (see for instance the index histograms in Refs. [14]). A high statistics study only found a tiny deviation, which tends to vanish in the large volume limit [62].

If we have data in the sectors up to charge Q , *i.e.* Q is the maximum of the simulated sectors $|\nu|$, we insert the measured values $\Sigma_0 \dots \Sigma_Q$, with the maximum and minimum of the statistical error bar. For higher charges we make use of inequality (5.3) to fix the minimal and maximal values as

$$\Sigma_{|\nu|,\min} = \frac{|\nu|}{mV} \quad , \quad \Sigma_{|\nu|,\max} = \Sigma_{|\nu|,\min} + \varepsilon_Q \quad . \quad (5.6)$$

In the cases $L = 24$ and 28 we do not have data for all the sectors with $|\nu| < Q$. Here we employ in addition inequality (5.4) and the results in the next smaller (larger) volume to fix $\Sigma_{|\nu|,\min}$ ($\Sigma_{|\nu|,\max}$).

If we insert some susceptibility χ_t into eq. (5.5), we obtain a value for Σ . Its uncertainty is modest, because most sectors, which have not been measured, have exponentially suppressed probabilities $p(|\nu|)$. By requiring agreement with the theoretical prediction of Ref. [6] (given in eq. (1.3)) we now determine χ_t ; the results are given in Table 9 and Figure 15.

Table 8 shows that only in the case of light fermions the prediction of Ref. [6] can be reproduced. For $L = 16$ and $m \geq 0.12$ *all* the Σ_ν are larger than the prediction, hence there is no way to reproduce it with a weighted sum. In the case $L = 32$, $m = 0.06$ the value of $\langle \Sigma_{\nu=0} \rangle$ is too close to the prediction for Σ to extract a sensible result for χ_t . At $L = 16$, $m = 0.09$ a value for χ_t which achieves this can still be found, but the result

L	m	Σ of Ref. [6]	χ_t	$\langle \nu^2 \rangle$
16	0.01	0.04888	0.0006586(5)	0.1686(1)
16	0.03	0.07050	0.00117(1)	0.299(3)
16	0.06	0.08883	0.00159(8)	0.407(20)
20	0.01	0.04888	0.000500(2)	0.200(1)
24	0.01	0.04888	0.000408(16)	0.235(9)
28	0.01	0.04888	0.000367(15)	0.288(12)
32	0.01	0.04888	0.000341(4)	0.349(4)

Table 9: Results for the topological susceptibility χ_t based on the method described in Subsection 5.1, which assumes Gaussian charge distribution and the chiral condensate according to Ref. [6]. On the $L = 16$ lattice this method does not work for $m \geq 0.09$, due to the latter assumption.

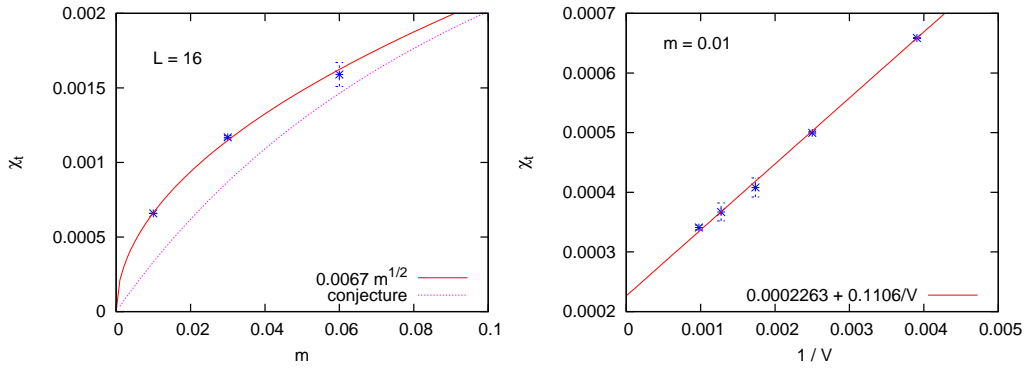


Figure 15: The topological susceptibility χ_t determined by the method described in Subsection 5.1. On the $L = 16$ lattice we see that Smilga's formula cannot be valid at $m \geq 0.09$, hence also this method is not applicable anymore. For the smaller masses our results for the susceptibility suggest a behaviour $\chi_t \propto \sqrt{m}$. It is compared to the conjecture in eq. (5.8), based on Refs. [18, 63]. The plot on the right refers to $m = 0.01$. An infinite volume extrapolation, which assumes χ_t to be consistent with a linear dependence on $1/V$, leads to $\chi_t = 0.0002263(53)$.

does not make sense either, since it is below the χ_t values determined at $m = 0.03$ and 0.06 (see Figure 15). We conclude that Smilga's formula is not applicable at $m \geq 0.09$, which assigns an explicit meaning to his assumption $m \ll 1/\sqrt{\beta} \simeq 0.45$.

Figure 15 (on the left) shows the consistency of our results with the behaviour

$$\chi_t(m) \propto \sqrt{m} . \quad (5.7)$$

Alternative results (with quenched configurations and re-weighting) were

given in Ref. [18]. On the theoretical side, Ref. [63] conjectured for N_f degenerate flavours in the large volume limit

$$\frac{1}{\chi_t} = \frac{N_f}{\Sigma^{(1)}m} + \frac{1}{\chi_{t,q}} , \quad \Sigma^{(1)} \simeq 0.160 g , \quad (5.8)$$

where $\Sigma^{(1)} := \Sigma_{N_f=1}(m=0)$ (cf. Section 1), and $\chi_{t,q} = \chi_t(m \rightarrow \infty)$ is the quenched value. Actually this mass dependence of χ_t was conjectured in the framework of QCD. If we apply the same form in the Schwinger model, and insert the value $\chi_{t,q} \approx 0.023 g^2 = 0.0046$ from Ref. [18], we obtain $\chi_t \approx 0.00033$. Figure 15 (on the left) shows a trend towards agreement with this conjecture as we increase the mass at $L = 16$, thus suppressing the finite size effects. In particular at $m = 0.06$ eq. (5.8) implies $\chi_t \simeq 0.0015$, close to our value in Table 9.

Also when we increase the volume at $m = 0.01$, our results attain the vicinity of this prediction: at $L = 32$ we obtained $\chi_t \approx 0.00034$, next to the predicted value ($\chi_t \approx 0.00033$).

If we try an infinite volume extrapolation, however, the plot in Figure 15 on the right suggests a linear dependence of χ_t on $1/V$; that assumption leads to a smaller value of $\chi_t(V = \infty) = 0.0002263(53)$.

5.2 An approximate formula for the topological summation

The procedure of the previous subsection is robust for light fermions (barring finite size effects on Σ). However, since it uses the analytic result for Σ as an input to determine χ_t , it does not evaluate Σ itself from the numerical results in distinct topological sectors. In Subsections 5.3 and 5.4 we will test a method to do so, following Ref. [64]. For convenience we re-derive here in a concise form the formula for an approximate topological summation that was given in Ref. [64] for the pion mass; we generalise it to arbitrary observables. This consideration follows the lines of Refs. [64, 65], pointing out in particular which assumptions are involved, so the subsequent subsections can refer to them.

First we assume the fermion field to be integrated out. Thus we refer to an effective gauge action $S_{\text{eff}}[U]$, which keeps track of the fermion determinant. So the partition function takes the form $Z = \int \mathcal{D}U \exp\{-S_{\text{eff}}[U]\}$. Next we introduce a Kronecker δ as a filter of gauge configurations $[U]$ with a specific topological charge ν ,

$$\delta_{\nu, \nu[U]} = \frac{1}{2\pi} \int_{-\pi}^{\pi} d\theta \exp\{i\theta(\nu - \nu[U])\} . \quad (5.9)$$

This formulation involves the vacuum angle θ , and it allows us to write a “partition function” restricted to one topological sector as

$$Z_\nu = \int \mathcal{D}U e^{-S_{\text{eff}}[U]} \delta_{\nu,\nu[U]} = \frac{1}{2\pi} \int_{-\pi}^{\pi} d\theta e^{i\theta\nu} Z(\theta) , \quad (5.10)$$

where $Z(\theta) = \int \mathcal{D}U \exp\{-S_{\text{eff}}[U] - i\theta\nu[U]\}$ is the (complete) partition function for a general vacuum angle (and $Z = Z(0)$).

If some observable \mathcal{O} is measured only in one topological sector, the corresponding expectation value is given by¹¹

$$\bar{\mathcal{O}}_\nu = \frac{1}{Z_\nu} \int \mathcal{D}U e^{-S_{\text{eff}}[U]} \delta_{\nu,\nu[U]} \mathcal{O}[U] = \frac{1}{2\pi Z_\nu} \int_{-\pi}^{\pi} d\theta e^{i\theta\nu} Z(\theta) \bar{\mathcal{O}}(\theta) . \quad (5.11)$$

The relation

$$-Z''(\theta)|_{\theta=0} = \langle \nu^2 \rangle = V\chi_t \quad (5.12)$$

suggests

$$Z(\theta) = Z \exp(-V\chi_t\theta^2/2) . \quad (5.13)$$

Inserting this ansatz into eq. (5.10) leads to

$$\frac{Z_\nu}{Z} = \frac{1}{2\pi} \int_{-\pi}^{\pi} d\theta \exp\left(-\frac{V\chi_t}{2}\theta^2 + i\theta\nu\right) , \quad (5.14)$$

where we recognise the stationary phase

$$\theta_{s,\nu} = i\frac{\nu}{V\chi_t} = i\frac{\nu}{\langle \nu^2 \rangle} . \quad (5.15)$$

As an approximation, we extend the bounds in the integral (5.14) to $\pm\infty$. For this step, it is favourable if $V\chi_t$ is large. Then we obtain

$$\frac{Z_\nu}{Z} \simeq \frac{1}{\sqrt{2\pi V\chi_t}} \exp\left(-\frac{\nu^2}{2V\chi_t}\right) . \quad (5.16)$$

This formula is obviously consistent with an integral approximation for $Z = \sum_\nu Z_\nu$, which is again best justified for large $V\chi_t$.

If we insert ansatz (5.13) into eq. (5.11), we obtain another integral with the stationary phase $\theta_{s,\nu}$. By repeating its approximation as a Gaussian integral, and employing relation (5.16), we arrive at

$$\begin{aligned} \bar{\mathcal{O}}_\nu &= \frac{Z}{2\pi Z_\nu} \int_{-\pi}^{\pi} d\theta \bar{\mathcal{O}}(\theta) \exp\left(-\frac{V\chi_t}{2}\theta^2 + i\theta\nu\right) \\ &\simeq \sqrt{\frac{V\chi_t}{2\pi}} \int_{-\infty}^{\infty} d\theta \bar{\mathcal{O}}(\theta) \exp\left(-\frac{V\chi_t}{2}(\theta - \theta_{s,\nu})^2\right) . \end{aligned} \quad (5.17)$$

¹¹We use the notation $\bar{\mathcal{O}}$, rather than $\langle \mathcal{O} \rangle$, because in the following this will be more practical for indicating the dependence on θ .

Since we assume only small $|\theta - \theta_{s,\nu}|$ to contribute significantly to this integral, we may also approximate

$$\bar{\mathcal{O}}(\theta) \simeq \bar{\mathcal{O}}(\theta_{s,\nu}) + \frac{1}{2} \bar{\mathcal{O}}''(\theta)|_{\theta_{s,\nu}} (\theta - \theta_{s,\nu})^2 . \quad (5.18)$$

Let us further assume $|\theta_s|$ to be small, so we can replace the first term in this formula for $\bar{\mathcal{O}}(\theta)$ by

$$\bar{\mathcal{O}}(\theta_{s,\nu}) \simeq \bar{\mathcal{O}}(0) + \frac{1}{2} \bar{\mathcal{O}}''(\theta)|_0 \theta_{s,\nu}^2 . \quad (5.19)$$

Hence a further property, which is favourable for our approximation, is a small topological charge $|\nu|$, in addition to a large value of $V\chi_t$.

The approximation (5.19) also implies $\bar{\mathcal{O}}''(\theta)|_{\theta_s} \simeq \bar{\mathcal{O}}''(\theta)|_0$. So we can express the (numerically measurable!) restricted expectation value as

$$\bar{\mathcal{O}}_\nu \simeq \sqrt{\frac{V\chi_t}{2\pi}} \int_{-\pi}^{\pi} d\theta \left[\bar{\mathcal{O}} + \frac{1}{2} \bar{\mathcal{O}}''[(\theta - \theta_{s,\nu})^2 + \theta_{s,\nu}^2] \right] \exp\left(-\frac{V\chi_t}{2}(\theta - \theta_{s,\nu})^2\right) , \quad (5.20)$$

where $\bar{\mathcal{O}}$ and $\bar{\mathcal{O}}''$ are taken at $\theta = 0$. Extending once more the boundaries to $\pm\infty$ leads to the final form

$$\bar{\mathcal{O}}_\nu \approx \bar{\mathcal{O}} + \frac{1}{2} \bar{\mathcal{O}}'' \frac{1}{V\chi_t} \left(1 - \frac{\nu^2}{V\chi_t}\right) . \quad (5.21)$$

This is the same structure as Ref. [64] obtained for the pion mass. It is consistent that the limit $V\chi_t \rightarrow \infty$ renders all topological sectors equivalent, so that all $\bar{\mathcal{O}}_\nu$ coincide with $\bar{\mathcal{O}}$.

The numerical measurement with few topological transitions provides results for the left-hand-side of eq. (5.21). On the right-hand-side $\bar{\mathcal{O}}$, $\bar{\mathcal{O}}''$ and χ_t are unknown. We are interested in $\bar{\mathcal{O}}$ and χ_t , and measurements of $\bar{\mathcal{O}}_\nu$ in various topological sectors and volumes allow in principle for their evaluation (as far as the above approximations make sense). Up to now, this intriguing and possibly powerful technique has not been tested with simulation data. This will be pioneered in the next two subsections.

5.3 Topological summation of the chiral condensate

Now we insert the chiral condensate Σ as our observable $\bar{\mathcal{O}}$. As our input we have data for some Σ_ν , *i.e.* for the left-hand-side of eq. (5.21), but on the right-hand side Σ , Σ'' and χ_t are unknown. In view of their evaluation, it is convenient to re-write eq. (5.21) as

$$\begin{aligned} \Sigma_\nu &\approx \Sigma - \frac{A}{V} + \frac{B}{V^2} \nu^2 \\ A &:= -\frac{\Sigma''}{2\chi_t} , \quad B := -\frac{\Sigma''}{2\chi_t^2} , \quad \chi_t = \frac{A}{B} . \end{aligned} \quad (5.22)$$

Based on data from different topological sectors in a fixed volume V we can only evaluate B ; it is not possible to obtain Σ and χ without including different volumes.

By considering two sectors with charges $|\nu| = k$ and ℓ (and $k \neq \ell$) at fixed V and m , a result for B is obtained as

$$\frac{1}{V} B_{k,\ell} = V \frac{\Sigma_k - \Sigma_\ell}{k^2 - \ell^2} = \frac{1}{m(k + \ell)} + V \frac{\varepsilon_k - \varepsilon_\ell}{k^2 - \ell^2}. \quad (5.23)$$

If more than two $\Sigma_{|\nu|}$ values have been measured, the approximate agreement between the emerging $B_{k,\ell}$ represents a consistency condition. In Table 10 we give corresponding results for $B_{k,\ell}/V$, derived from the data in Table 8.

m	L	$B_{1,0}/V$	$B_{2,0}/V$	$B_{2,1}/V$	$B_{3,0}/V$	$B_{4,0}/V$
0.01	32	95.33(55)	48.44(16)	32.80(15)		
0.12	16	2.59(18)	1.882(50)	1.647(48)		
0.18	16	0.90(11)	0.730(32)	0.674(43)		
0.24	16	0.49(11)	0.410(36)	0.384(38)	0.356(28)	0.333(13)

Table 10: *Results for the term $B_{k,\ell}/V$ obtained in each case from two values of $\Sigma_{|\nu|}$ in a fixed volume V and at a fixed mass m , according to eq. (5.23).*

For small fermion masses, the results for $B_{k,\ell}$ are dominated by the semi-classical term $1/[m(k + \ell)]$, and thus strongly dependent on the topological sectors involved. This feature is suppressed, however, when m increases; in particular for $L = 16$, $m = 0.24$ we do observe approximate agreement for different choices of k and ℓ , in striking contrast to the semi-classical result. This similarity, which is illustrated in Figure 16, is a remarkable quantum effect, due to the fluctuation terms $\varepsilon_{|\nu|}$. Still we observe systematically that the $B_{k,\ell}$ values decrease if higher topological charges are involved. That also reduces the reliability of our assumption of a small $|\theta_{s,\nu}|$ — which favours the approximation (5.19) — so we consider $B_{1,0}$ most reliable.

In order to proceed, *i.e.* to get access also to A and thus to χ and Σ , we have to confront data from different volumes. Considering two volumes V_1 and V_2 , but keeping m and $|\nu|$ fixed, eq. (5.22) implies

$$\Sigma_{|\nu|}(V_1) - \Sigma_{|\nu|}(V_2) = A \left(\frac{1}{V_2} - \frac{1}{V_1} \right) + B\nu^2 \left(\frac{1}{V_1^2} - \frac{1}{V_2^2} \right). \quad (5.24)$$

Most convenient is the sector $\nu = 0$, where we can read off A without involving the variable B . At $|\nu| = 1$ it is most obvious to insert B as

$$\Sigma_1(V_1) - \Sigma_1(V_2) = A \left(\frac{1}{V_2} - \frac{1}{V_1} \right) + \frac{B_{1,0}(V_1)}{V_1^2} - \frac{B_{1,0}(V_2)}{V_2^2}, \quad (5.25)$$

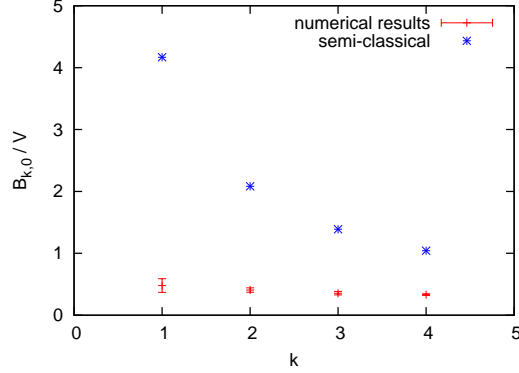


Figure 16: The terms $B_{k,0}/V$ for $k = 1 \dots 4$, at $m = 0.24$, $L = 16$. For the numerical result we observe a remarkable stability in k , in contrast to the semi-classical values.

which is identical to the result obtained from $\Sigma_0(V_1)$, $\Sigma_0(V_2)$. This is expected to be the most reliable value for A . Our results obtained in this way are listed in Table 11.

m	$m = 0.01$			$m = 0.06$
(L_1, L_2)	(20, 16)	(32, 16)	(32, 20)	(32, 16)
A	0.974(221)	1.833(173)	2.626(383)	5.803(363)

Table 11: Results for the term A in eq. (5.22), obtained from Σ_0 or Σ_1 in two volumes, at a fixed mass m , according to eqs. (5.24) and (5.25).

The idea is to use these results in both volumes involved. This is sensible if A is approximately constant in the volume, but that is not confirmed in our data set for $m = 0.01$. Since the assumptions tend to hold better for larger volumes, we use the value of A obtained in $(L_1, L_2) = (32, 16)$ to determine Σ in $L = 16$, and A from $(32, 20)$ for Σ in $L = 20$ and 32. This leads to

$$\Sigma \simeq 0.0199(7) \quad (L = 16), \quad \Sigma \simeq 0.0207(12) \quad (L = 20 \text{ or } 32). \quad (5.26)$$

These results for Σ are nicely consistent, but more than a factor of 2 below the value expected in infinite volume. Hence for $m = 0.01$ this method works in an intrinsically consistent way, but the results for Σ are reduced by strong finite size effects.

Similarly, if we now evaluate χ_t by referring to eq. (5.22) we obtain values between 10^{-5} and 10^{-4} , *i.e.* well below the results in Subsection 5.1. Note that the applicability of the method used here — based on the

approximations in Subsection 5.2 — is indeed questionable for $m = 0.01$, since we are dealing with a small value of $V\chi_t$.

So the mass $m = 0.06$ is more promising. We cannot test the volume independence of A from our data, but based on $L = 16$ and 32 we obtain

$$m = 0.06 \quad : \quad A = 5.80(36) \, , \quad \Sigma = 0.0940(16) \, . \quad (5.27)$$

Let us focus on the size $L = 32$ and involve $B_{1,0}$, which leads to

$$\chi_t = 0.00118(30) \, . \quad (5.28)$$

The method that we used in Subsection 5.1 to evaluate χ_t does not work in this case as we mentioned before (due to the sizable uncertainty of Σ_1 it basically just constrains $\chi_t < 0.03$). However, if we now insert the preferred value $\chi_t \simeq 0.00118$ and evaluate Σ by topological summation, we arrive at

$$\Sigma = 0.0883(69) \, . \quad (5.29)$$

This result is in excellent agreement with the analytical predictions based on Ref. [6], $\Sigma = 0.08883$.

We conclude that some consistency tests are passed well. However, for $m = 0.01$ the ultimate results for χ_t and the Σ (summed over all topological sectors) seem to be affected by strong finite size effects.

The situation improves as we proceed to $m = 0.06$. In this case the correlation length (in infinite volume) is only 4.2 lattice spacings, so that the finite size effects are suppressed quite well, and we arrive at sensible results for χ_t and Σ .

5.4 Topological summation of the “pion” mass

For practical reasons, it is favourable to consider the decay of a current correlation function for measurements of the “pion” mass, rather than the pseudoscalar density [7]. In this way we obtained the results in Table 12.

Again we can test the topological summation for the fermion masses $m = 0.01$ and 0.06 . Here we proceed in a manner different from Subsection 5.3: if we insert the data of Table 12 into the formula

$$M_{\pi,|\nu|} = M_\pi - \frac{A}{V} + \frac{B}{V^2}\nu^2 \, , \quad (5.30)$$

the unknown terms M_π , A and B are over-determined. We choose the optimal values for them by a least square fit.

Let us start again with $m = 0.01$: if we include all 11 sector that we simulated, we obtain $M_\pi = 0.115(3)$, and if we skip the 4 sectors with

L	m	$M_{\pi,0}$	$M_{\pi,1}$	$M_{\pi,2}$	$M_{\pi,3}$	$M_{\pi}^{\text{theory}}(L = \infty)$
16	0.01	0.041(1)	0.271(4)			0.071
16	0.03	0.123(5)	0.275(4)			0.148
16	0.06	0.214(6)	0.310(3)			0.235
16	0.09	0.302(5)	0.358(2)			0.308
16	0.12	0.359(5)	0.413(2)	0.494(5)		0.374
16	0.18	0.498(4)	0.525(2)	0.589(5)		0.490
16	0.24	0.631(6)	0.648(2)	0.700(3)		0.593
20	0.01	0.038(2)	0.209(4)			0.071
24	0.01			0.257(8)	0.32(1)	0.071
28	0.01		0.146(4)		0.25(1)	0.071
32	0.01	0.05(1)	0.160(8)	0.192(6)		0.071
32	0.06	0.23(1)	0.232(7)			0.235

Table 12: The “pion” masses measured in various volumes, at different fermion masses, in the topological sectors $|\nu| = 0 \dots 3$. The last column displays the (infinite volume) prediction of Ref. [6] (cf. eq. (1.4)).

$|\nu| > 1$ (which are problematic for our approximations) the result is slightly reduced to $M_{\pi} = 0.113(4)$. Thus we confirm the observation of Subsection 5.3 that the summation formula runs into trouble for this light mass. Actually this is not surprising: we recall that the correlation length for this fermion mass (in infinite volume) is $\xi \simeq 14$, cf. Figure 4, hence strong finite size effects are expected, and they generically enhance the mass gap.

Therefore, we now skip the smallest volumes. We need at least two volumes to determine the term A , so we restrict the consideration to $L = 28$ and 32, and we include $|\nu| \leq 2$; thus we are left with four sectors. This small number of input data causes a large error, but the optimal value of the least square fit moves very close to the theoretical prediction (see Table 12),

$$m = 0.01 \quad : \quad M_{\pi} = 0.073(25) \quad .$$

For $m = 0.06$ we only have four sectors to deal with, but the finite size effects are much less severe, and we arrive again at a sensible result,

$$m = 0.06 \quad : \quad M_{\pi} = 0.232(8) \quad , \quad \chi_t = 0.0007(4) \quad . \quad (5.31)$$

As we already saw in Subsection 5.3, this method is not very useful for the determination of χ_t ; it is always plagued by a large uncertainty, as in the example given here (for $m = 0.01$ this is even worse). The three results that we obtained for χ_t at $m = 0.06$ (in Subsection 5.1, 5.3 and 5.4) differ within the same magnitude.¹²

¹²The result in Table 9 is larger, but only based on $L = 16$.

Regarding the “pion” mass, we confirm that this method can work, if it is applied in an appropriate regime. Hence this approach may in fact be promising for further applications, including QCD, if finite size effects are under control — in particular the term $\langle \nu^2 \rangle$ should not be too small.

5.5 Correlation of the topological charge density

Members of the JLQCD Collaboration proposed an alternative method to evaluate χ_t even in one single topological sector based on the topological charge *density*, $\rho_t(x)$. Ref. [65] derived the “model independent formula”

$$\lim_{|x| \rightarrow \infty} \langle \rho_t(x) \rho_t(0) \rangle_{|\nu|} \simeq -\frac{\chi_t}{V} + \frac{1}{V^2} \left(\nu^2 + \frac{c_4}{2\chi_t} \right) + O(V^{-3}) , \quad (5.32)$$

which captures even a possible deviation from the Gaussian charge distribution by a non-vanishing kurtosis $c_4 = (\langle \nu^4 \rangle - 3\langle \nu^2 \rangle)/V$.¹³ However, this term is known to be tiny, so we neglect it in the following.

The issue is to search for a plateau value of the charge density correlation at large distances, which differs from the constant ν^2/V^2 (in the sector with topological charge $|\nu|$). This shift $\Delta = -\chi_t/V$ is negative because fluctuations in $\rho_t(x)$ have to compensate. However, Δ tends to be small and hard to resolve numerically. For the absolute value $|\Delta|$ it is favourable if m increases (although we are actually interested in quasi-chiral fermions), but it is unfavourable if V increases (although we need access to the asymptotic value in eq. (5.32), and $O(V^{-3})$ should be negligible). Moreover, in analogy to the approximations that lead to eq. (5.21), the derivation of eq. (5.32) involves the assumptions

$$\langle \nu^2 \rangle = V\chi_t \text{ is large , } \quad \frac{|\nu|}{\langle \nu^2 \rangle} \text{ is small .} \quad (5.33)$$

Our estimates for χ_t suggest that we do not have any setting which is really adequate for the first of these two conditions. Sometimes, however, such approximations apply reasonably well even if the assumptions do not strictly hold (this is the experience in QCD with simulation data matched to formulae of the ϵ - or δ -regime, and in the preceding two subsections to some extent).

Since our configurations are smooth, it is not problematic to use the naive lattice formulation of the topological charge density, $\rho_t = \epsilon_{12} F_{12}$. (There is a cleaner formulation for Ginsparg-Wilson fermions [25], but it is tedious in practice.) As examples, the results for $L = 16$ in the topologically neutral sector for three masses are shown in Figure 17. In particular

¹³A variant of this method, which uses the η' -correlation of the pseudo-scalar density, has been applied to two-flavour QCD in Ref. [66].

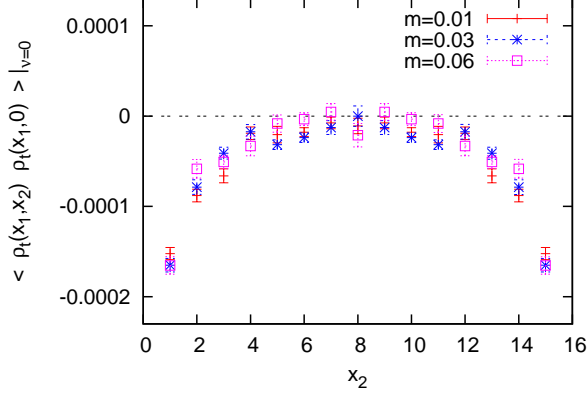


Figure 17: *The topological charge correlation function for $L = 16$, $\nu = 0$ and $m = 0.01, 0.03$ and 0.06 .*

we see that the correlation over short (but non-vanishing) distances is negative, since a given link variable contributes with opposite signs to ρ_t in its adjacent plaquettes. The jackknife errors for the quantity $\langle \rho_t(x) \rho_t(0) \rangle_0$ are typically in the range $(1 \dots 2) \cdot 10^{-5}$.

In the most promising case, $m = 0.06$, we evaluated 741 topologically neutral configurations and we have identified the magnitude for $\chi_t \approx 0.0015$ which implies $\Delta \approx -6 \cdot 10^{-6}$. In order to safely resolve this shift we would therefore need about 50 000 to 100 000 configurations. We conclude that this method requires a very large statistics, so we cannot apply it.

6 Conclusions

We presented a study of the 2-flavour Schwinger model with dynamical chiral fermions. We applied the overlap Hypercube Fermion (HF), and confirmed its features as a promising formulation of a chiral lattice fermion. This is manifest by its excellent locality and scaling behaviour. Moreover, our study allowed us to explore a number of conceptually interesting and relevant issues, and to test new methods to handle them.

This is certainly of interest, even in a toy model, since simulations with dynamical overlap fermions have been explored only poorly so far.

For our simulation we designed a specifically suitable variant of the Hybrid Monte Carlo (HMC) algorithm, demonstrated its correctness and tested its efficiency. It is sufficient to insert a low polynomial approximation for the overlap operator to compute the force term, while the high precision overlap operator is employed in the accept/reject step. It is an open question if this strategy — perhaps with further refinements — can

be carried over to the simulation of QCD with dynamical chiral quarks.

Next we discussed the spectrum of the Dirac operator. Random Matrix Theory is not yet worked out for this type of model, with a vanishing chiral condensate at zero fermion mass. Nevertheless the unfolded level spacing density follows the standard RMT formula for the unitary ensemble.

The prediction $\Sigma(m) \propto m^{1/3}$ [4–6] suggests a microscopic spectral density $\rho(\lambda \gtrsim 0) \propto \lambda^{1/3}$, and the scale-invariant variable $\zeta \propto \lambda V^{3/4}$ (if we assume no explicit mass dependence of ρ). This conjecture does, however, not agree with our data. An alternative scenario with $\rho(\lambda \gtrsim 0) \propto \lambda^{1/2}$ has a theoretical background as well (Gaussian distribution), but the data do not really support it either. Instead they favour $z \propto \lambda V^{5/8}$ as the scale-invariant variable, and therefore $\rho(\lambda \gtrsim 0) \propto \lambda^{3/5}$.

A hint for an interpretation of this surprising result can be found in Ref. [5], which derived the behaviours $\Sigma \propto m^{1/3}$ and $\Sigma \propto mL$ in two limiting cases. Regarding the parameter that characterises these extreme cases, our settings are in an intermediate regime, which appears compatible with the relation $\Sigma \propto m^{3/5}$ that we observed. For a precise theoretical clarification, we hope for the corresponding RMT formulae to be elaborated.

Direct measurements of the chiral condensate and of the mass of the isotriplet (“pion”) could only be performed in fixed topological sectors, since the HMC histories contain only few topological transitions. This limitation is generic for the simulation of light fermions close to the continuum limit. It is therefore a major challenge to explore techniques for the topological summation of such measurements. Assuming a Gaussian distribution of the topological charges, the data can be used to evaluate the topological susceptibility. In order to determine the actual observable, we explored approximate summation techniques, which led to sensible results in some parameter window, where the term $\langle \nu^2 \rangle = V\chi_t$ is not too small.

Topological summations could become relevant for future QCD simulations. Nowadays they are carried out with very light dynamical quarks — such that the pion mass is close to its physical value — on finer and finer lattices. In particular in applications of dynamical overlap fermions [17] the HMC history tends to be trapped in the topologically trivial sector for the entire simulation, which endangers ergodicity and does not provide the physical result (unless the volume is very large). For Wilson-type lattice fermions (which break the chiral symmetry explicitly), the problem is less obvious on the currently used lattice spacings, but on still finer lattices (with $a \lesssim 0.05$ fm) it is expected to show up as well [22]. Hence topological summation methods are of interest for non-perturbative studies of low energy nuclear physics based on first principles of QCD. Our results tell us

to be cautious with such summations, but at the same time they provide hope for their feasibility.

Acknowledgements We are indebted to Martin Hasenbusch for helpful advice on algorithmic aspects, to Poul Damgaard and Jacques Verbaarschot for sharing their deep insight into Random Matrix Theory, and to Stephan Dürr, Hidenori Fukaya and Jim Hetrick for very useful comments. Most production runs were performed on the clusters of the “Norddeutscher Verbund für Hoch- und Höchstleistungsrechnen” (HLRN). We thank Hinnerk Stüben for technical assistance, as well as Edwin Laermann and Michael Müller-Preußker for their support at Bielefeld and Humboldt University, respectively. This work was supported in part by the Croatian Ministry of Science, Education and Sports (project No. 0160013), and by the Deutsche Forschungsgemeinschaft (DFG) through Sonderforschungsbereich Transregio 55 (SFB/TR55) “Hadron Physics from Lattice QCD”, which is coordinated by the University of Regensburg.

References

- [1] J. Schwinger, *Phys. Rev.* **128** (1962) 2425. S.R. Coleman, R. Jackiw and L. Susskind, *Annals Phys.* **93** (1975) 267. S.R. Coleman, *Annals Phys.* **101** (1976) 239.
- [2] Y. Hosotani, R. Rodriguez, J.E. Hetrick and S. Iso, [hep-th/9606129](#).
- [3] D. Mermin and H. Wagner, *Phys. Rev. Lett.* **17** (1966) 1133. P.C. Hohenberg, *Phys. Rev.* **158** (1967) 383. S.R. Coleman, *Commun. Math. Phys.* **31** (1973) 259.
- [4] A.V. Smilga, *Phys. Lett. B* **278** (1992) 371.
- [5] J.E. Hetrick, Y. Hosotani and S. Iso, *Phys. Lett. B* **350** (1995) 92.
- [6] A.V. Smilga, *Phys. Rev. D* **55** (1997) 443.
- [7] C. Gattringer, I. Hip and C.B. Lang, *Phys. Lett. B* **466** (1999) 287.
- [8] M. Gell-Mann, R.J. Oakes and B. Renner, *Phys. Rev.* **175** (1968) 2195.
- [9] T. Banks and A. Casher, *Nucl. Phys. B* **169** (1980) 103. A review for various lattice fermion formulations is given in M. Creutz, [arXiv:hep-lat/0511052](#).
- [10] T. Wilke, T. Guhr and T. Wettig, *Phys. Rev. D* **57** (1998) 6486.

- [11] S.M. Nishigaki, P.H. Damgaard and T. Wettig, *Phys. Rev. D* **58** (1998) 087704. P.H. Damgaard and S.M. Nishigaki, *Nucl. Phys. B* **518** (1998) 495; *Phys. Rev. D* **63** (2001) 045012.
- [12] W. Bietenholz, K. Jansen and S. Shcheredin, *JHEP* **07** (2003) 033.
- [13] L. Giusti, M. Lüscher, P. Weisz and H. Wittig, *JHEP* **11** (2003) 023. D. Galletly *et al.* (QCDSF-UKQCD Collaboration), *Nucl. Phys. (Proc. Suppl.)* **B 129** (2004) 456.
- [14] W. Bietenholz and S. Shcheredin, *Nucl. Phys. B* **754** (2006) 17. S. Shcheredin, Ph.D. Thesis [[hep-lat/0502001](#)]. W. Bietenholz, Habilitation Thesis, *Fortschr. Phys.* **56** (2008) 107.
- [15] P.H. Damgaard, *Phys. Lett. B* **608** (2001) 162.
- [16] T. DeGrand, R. Hoffmann, S. Schäfer and Z. Liu, *Phys. Rev. D* **74** (2006) 054501. T. DeGrand, Z. Liu and S. Schäfer, *Phys. Rev. D* **74** (2006) 094504. T. DeGrand and S. Schäfer, *Phys. Rev. D* **76** (2007) 094509.
- [17] H. Fukaya *et al.* (JLQCD Collaboration), *Phys. Rev. Lett.* **98** (2007) 172001; *Phys. Rev. D* **76** (2007) 054503; *Phys. Rev. D* **77** (2008) 074503. S. Aoki *et al.* (JLQCD and TWQCD Collaboration), *Phys. Rev. D* **80** (2009) 034508. J. Noaki *et al.*, *Phys. Rev. D* **81** (2010) 034502. H. Fukaya *et al.* (JLQCD and TWQCD Collaboration), *Phys. Rev. D* **83** (2011) 074501.
- [18] S. Dürr and C. Hoelbling, *Phys. Rev. D* **71** (2005) 054501.
- [19] P.H. Damgaard, U.M. Heller, R. Narayanan and B. Svetitsky, *Phys. Rev. D* **71** (2005) 114503.
- [20] C.B. Lang and T.K. Pany, *Nucl. Phys. B* **513** (1998) 645.
- [21] A. Bode, U.M. Heller, R.G. Edwards and R. Narayanan, in Proceedings of the Workshop “Lattice Fermions and Structure of the Vacuum”, Dubna (Russia), Kluwer Academic C553 (2000) p. 65 (eds. V. Mitrjushkin and G. Schierholz) [[hep-lat/9912043](#)].
- [22] M. Lüscher, *Commun. Math. Phys.* **293** (2010) 899; *JHEP* **1008** (2010) 071; *PoS(LATTICE2010)* 015.
- [23] J. Volkholz, W. Bietenholz and S. Shcheredin, *PoS(LAT2006)*040. W. Bietenholz, S. Shcheredin and J. Volkholz, *PoS(LAT2007)*064. W. Bietenholz and I. Hip, *PoS(LAT2008)*079; *PoS(LAT2009)*086.

- [24] W. Bietenholz and U.-J. Wiese, *Nucl. Phys.* **B 464** (1996) 319.
- [25] M. Lüscher, *Phys. Lett.* **B 428** (1998) 342.
- [26] P.H. Ginsparg and K.G. Wilson, *Phys. Rev.* **D 25** (1982) 2649.
- [27] U.-J. Wiese, *Phys. Lett.* **B 315** (1993) 417. W. Bietenholz and U.-J. Wiese, *Nucl. Phys. (Proc. Suppl.)* **B 34** (1994) 516; *Phys. Lett.* **B 378** (1996) 222.
- [28] P. Hasenfratz, *Nucl. Phys. (Proc. Suppl.)* **B 63** (1998) 53. P. Hasenfratz, V. Laliena and F. Niedermayer, *Phys. Lett.* **B 427** (1998) 125. P. Hasenfratz, *Nucl. Phys.* **B 525** (1998) 401.
- [29] D.B. Kaplan, *Phys. Lett.* **B 288** (1992) 342. Y. Shamir, *Nucl. Phys.* **B 406** (1993) 90.
- [30] Y. Kikukawa and H. Neuberger, *Nucl. Phys.* **B 513** (1998) 735.
- [31] H. Neuberger, *Phys. Lett.* **B 417** (1998) 141; *Phys. Lett.* **B 427** (1998) 353.
- [32] W. Bietenholz, R. Brower, S. Chandrasekharan and U.-J. Wiese, *Nucl. Phys. (Proc. Suppl.)* **B 53** (1997) 921.
- [33] W. Bietenholz, *Eur. Phys. J.* **C 6** (1999) 537.
- [34] W. Bietenholz and I. Hip, *Nucl. Phys.* **B 570** (2000) 423; *Nucl. Phys. (Proc. Suppl.)* **B 83** (2000) 600.
- [35] J. van den Eshof, A. Frommer, Th. Lippert, K. Schilling and H.A. van der Vorst, *Comput. Phys. Commun.* **146** (2002) 203.
- [36] P. Hernández, K. Jansen and M. Lüscher, *Nucl. Phys.* **B 552** (1999) 363.
- [37] W. Bietenholz, in Proceedings of the “International Workshop on Non-Perturbative Methods and Lattice QCD”, Guangzhou (China), World Scientific (Singapore, 2001) p. 3 (eds. X.-Q. Luo and E.B. Gregory) [[hep-lat/0007017](#)]; *Nucl. Phys.* **B 644** (2002) 223.
- [38] Z. Fodor, *PoS(CPOD07)027*.
- [39] S. Shcheredin and E. Laermann, *PoS(LAT2006)146*.
- [40] P. Hasenfratz and F. Niedermayer, *Nucl. Phys.* **B 414** (1994) 785.

- [41] N. Christian, K. Jansen, K.-I. Nagai and B. Pollakowski, *Nucl. Phys.* **B 739** (2006) 60.
- [42] L. Giusti, C. Hoelbling, M. Lüscher and H. Wittig, *Comput. Phys. Commun.* **153** (2003) 31.
- [43] W. Bietenholz, T. Chiarappa, K. Jansen, K.-I. Nagai and S. Shcheredin, *JHEP* **0402** (2004) 023. H. Fukaya, S. Hashimoto and K. Ogawa, *Prog. Theor. Phys.* **114** (2005) 451.
- [44] L. Giusti, P. Hernández, M. Laine, P. Weisz and H. Wittig, *JHEP* **0401** (2004) 003.
- [45] W. Bietenholz *et al.* (QCDSF Collaboration), *Phys. Lett. B* **687** (2010) 410; *J. Phys. Conf. Ser.* **287** (2011) 012016.
- [46] S. Duane, A.D. Kennedy, B.J. Pendleton and D. Roweth, *Phys. Lett. B* **195** (1987) 216.
- [47] I. Montvay and G. Münster, “Quantum Fields on a Lattice”, Cambridge University Press, Cambridge UK (1994), Section 7.6. A.D. Kennedy, [hep-lat/0607038](#). M. Lüscher, [arXiv:1002.4232 \[hep-lat\]](#).
- [48] Z. Fodor, S.D. Katz and K.K. Szabo, *JHEP* **0408** (2004) 003. G.I. Egri, Z. Fodor, S.D. Katz and K.K. Szabo, *JHEP* **0601** (2006) 049.
- [49] N. Cundy, S. Krieg, Th. Lippert and A. Schäfer, *Comput. Phys. Commun.* **180** (2009) 201.
- [50] W. Bietenholz and H. Dilger, *Nucl. Phys.* **B 549** (1999) 335.
- [51] J.C. Sexton and D.H. Weingarten, *Nucl. Phys.* **B 380** (1992) 363.
- [52] N. Christian, K. Jansen, K.-I. Nagai and B. Pollakowski, *PoS(LAT2005)239*.
- [53] R.G. Edwards, I. Horváth and A.D. Kennedy, *Nucl. Phys.* **B 484** (1997) 375. C. Liu, A. Jaster and K. Jansen, *Nucl. Phys.* **B 524** (1998) 603. B. Joo, B. Pendleton, A.D. Kennedy, A.C. Irving, J.C. Sexton, S.M. Pickles, S.P. Booth (UKQCD Collaboration), *Phys. Rev. D* **62** (2000) 114501.
- [54] S. Dimopoulos, *Nucl. Phys.* **B 168** (1980) 69. M.E. Peskin, *Nucl. Phys.* **B 175** (1980) 197. J.P. Preskill, *Nucl. Phys.* **B 177** (1981) 21.
- [55] W. Bietenholz, *Int. J. Mod. Phys. A* **25** (2010) 1699.

- [56] M.A. Halasz and J.J.M. Verbaarschot, *Phys. Rev. Lett.* **74** (1995) 3920.
- [57] R.G. Edwards, U.M. Heller, J.E. Kiskis and R. Narayanan, *Phys. Rev. Lett.* **82** (1999) 4188.
- [58] P.H. Damgaard, U.M. Heller, R. Niclasen and K. Rummukainen, *Nucl. Phys. B* **583** (2000) 347.
- [59] F. Farchioni, P. de Forcrand, I. Hip, C.B. Lang and K. Splittorff, *Phys. Rev. D* **62** (2000) 014503. T. Kovács, *Phys. Rev. Lett.* **104** (2010) 031601.
- [60] H. Leutwyler and A. Smilga, *Phys. Rev. D* **46** (1992) 5607.
- [61] P.H. Damgaard, private communication.
- [62] S. Dürr, Z. Fodor, C. Hoelbling and T. Kurth, *JHEP* **0704** (2007) 055.
- [63] S. Dürr, *Nucl. Phys. B* **611** (2001) 281, and private communication.
- [64] R. Brower, S. Chandrasekharan, J.W. Negele and U.-J. Wiese, *Phys. Lett. B* **560** (2003) 64.
- [65] S. Aoki, H. Fukaya, S. Hashimoto and T. Onogi, *Phys. Rev. D* **76** (2007) 054508.
- [66] S. Aoki *et al.* (JLQCD and TWQCD Collaborations), *Phys. Lett. B* **665** (2008) 294.